

# Nonequilibrium dynamics of suppression, revival, and loss of charge order in a laser-pumped electron-phonon system

Sankha Subhra Bakshi<sup>1</sup>, Debraj Bose<sup>1</sup>, Arijit Dutta<sup>2</sup> and Pinaki Majumdar<sup>1</sup>

<sup>1</sup> Harish-Chandra Research Institute (A CI of Homi Bhabha National Institute), Chhatnag Road, Jhusi, Allahabad 211019

<sup>2</sup> Institut für Theoretische Physik, Goethe-Universität, 60438 Frankfurt am Main, Germany

(Dated: May 16, 2024)

An electron-phonon system at commensurate filling often displays charge order (CO) in the ground state. Such a system subject to a laser pulse shows a wide variety of behaviour. A weak pulse sets up low amplitude oscillations in the order parameter, with slow decay to a slightly suppressed value. A strong pulse leads to destruction of the charge order with the order parameter showing rapid, oscillatory, decay to zero. The regime in between, separating the weak pulse CO sustained state from the strong pulse CO destroyed state, shows an initial rapid decay of the order parameter, followed by a low amplitude quiescent state, and the rise to a finite steady state value over a timescale  $\tau_{cr}$ . The steady state value goes to zero and  $\tau_{cr}$  diverges as the pulse amplitude is increased towards a critical strength. We provide a complete characterisation of the dynamics in this nonequilibrium problem for varying electron-phonon coupling and pulse strength, highlight the multiple gap closing and opening transitions that occur, and suggest a simple dynamical model incorporating the pulse induced nonequilibrium electron population.

## I. INTRODUCTION

Recent experiments have started to explore the quantum dynamics in correlated electron systems [1–20]. The method involves imparting energy to the electron system via an electromagnetic pulse and studying the evolution by probing time dependence of the photoemission spectra or optical conductivity [21–26]. Although all experimental systems are in some thermal environment, at short enough time the pulse driven systems probe quantum states at energies much higher than what temperature alone would allow. To that extent one probes “athermal” dynamics. The excess energy imparted by the pulse can lead to various nonequilibrium phenomena including melting of order [3–10], the emergence of new order [11–14], and “transitions” in transport and optical behaviour [6, 9] - all of these arising from a non thermal population of excitations.

For systems coupled to a thermal bath, at long time the added energy is dissipated and one attains the equilibrium state, but the transient dynamics can be very interesting. For a system that is nominally thermally isolated, i.e. cannot dissipate the added energy, neither the transient nor the steady state is known a priori. In particular, one key question is whether the long time state admits an equilibrium description with an effective temperature. Finally, a system that is periodically driven can display steady states which do not have an equilibrium counterpart [27–29].

Our focus is on the dynamics in a “thermally isolated” charge ordered electron-phonon (EP) system subject to a laser pulse, and the spatio-temporal dynamics that arises as a result. One expects that as the added energy increases the charge order will be progressively suppressed, and ultimately destroyed. That is indeed the answer at long times. What is far less obvious is the dynamics associated with this process. This paper provides a real space, real time, description of this process and suggests a phenomenology to explain the microscopic answers. Before summarising our method and key results we touch upon what is known about the equilibrium charge ordered state in EP systems, and what recent pump-

probe experiments have revealed about dynamics.

Strong electron-phonon interaction leads to the formation of an electron-phonon bound state - the lattice polaron - which serves as the basic degree of freedom at strong coupling [30–32]. At commensurate electron filling the polarons can order into a ‘charge ordered’ (CO) state, involving periodic modulation of the bond lengths and electron density [33, 34]. The equilibrium physics of such CO systems is well understood [35–38].

Recent experimental advances allow strong perturbation of the CO state by application of a laser pulse (the ‘pump’) and probe the resulting electron-phonon dynamics via time and angle resolved photoemission spectroscopy (trARPES) [18, 22–24] or resonant inelastic x-ray scattering (RIXS) [25, 26]. The pump adds excess energy to the electrons which, due to the presence of EP interaction, gets transferred in part to the lattice. As a result, suppression and eventually melting of charge order can be observed. Such experiments have been done on 1T-TaS<sub>2</sub> [10], tritellurides [19] and the cuprates [26] in their charge ordered phases. Depending on the strength of the photo-excitation the following features are observed. (i) Weak photo-excitation leads to a damped periodic modulation of the electronic gap as well as the electronic temperature [19, 26]. (ii) With increasing photo-excitation one sees dynamics where the charge order vanishes at short times and then recovers slowly to a suppressed value. This is accompanied by an insulator-metal-insulator transitions as a function of time [16, 17]. (iii) At strong photo-excitation the CO melts rapidly resulting in an insulator-metal (I-M) transition [15, 20].

The dynamics in response to a weak pump pulse can be understood via linear response theory [39, 40], along with the system’s response to a probe pulse [41–43]. However, the strongly perturbed system displays dynamics that require the solution of the full time-dependent problem. For this, one can employ a phenomenological time-dependent Ginzburg-Landau theory [44, 45], or fully microscopic approaches.

The microscopic difficulty is in handling widely different electron and phonon timescales at strong coupling. For EP

systems methods like exact diagonalization (ED) [46] and dynamical mean field theory (DMFT) [47, 48] provide accurate results on electronic timescales but cannot access the real space correlations. ED calculations are severely limited by system size.

Given the energy scale difference between electrons and phonons in the adiabatic regime, and the related need to retain a large tower of phonon states, the approach could be to treat the phonons classically. This approach has been used within a Monte Carlo scheme recently to explain the ringing in the EP system on photoexcitation [49]. The method still requires iterative diagonalization to evolve the system

and for a large system size diagonalization even for ‘non interacting’ electrons become too costly to capture the rich dynamics of the order parameter. Our method, below, allows access to ‘long times’ at modest computational cost and captures all the key features of order parameter dynamics in a charge ordered system.

We use a ‘‘mean field dynamics’’ (MFD) scheme to study the dynamics of the CO state in the half-filled (spinless) Holstein model in two dimensions. We set up coupled equations of motion for the expectation values of the phonon displacement operator  $\hat{x}_i(t)$  and the electron bilinear  $\hat{\rho}_{ij}(t) = c_i^\dagger(t)c_j(t)$ . The equations close when one factorises the electron-phonon interaction term. This is a  $\mathcal{O}(N^2)$  process for each time step and the number of timesteps required range from  $10^6$  to  $10^8$ . Despite its apparent simplicity the method captures the effect of strong EP coupling and spatial correlations accurately. It goes beyond the ‘static phonon’ (or adiabatic) approximation, widely used before [50]. An approach similar to ours has been used recently to study the double exchange model [51].

We work at intermediate EP coupling (below the single polaron threshold) and probe the pulse strength ( $E_0$ ) dependence of the dynamics. Our primary indicators are the phonon amplitude at the ordering wavevector,  $x_{\mathbf{Q}}(t)$ , and the charge density wave field  $n_{\mathbf{Q}}(t)$ , where  $\mathbf{Q} = (\pi/a_0, \pi/a_0)$  on our square lattice with spacing  $a_0$ . We set  $a_0 = 1$ . Our main results are the following:

(1). *Long time state*: With increasing pulse amplitude  $E_0$  the long time state attained by the system changes from charge ordered to charge disordered at a critical amplitude  $E_0^c$ . At the EP coupling where we study the problem  $E_0^c$  also demarcates a gap closing transition in the long time electronic state.

(2). *Transient response*: There are three regimes in terms of pulse strength: (i) For  $E_0 \ll E_0^c$  the indicators  $|x_{\mathbf{Q}}|$  and  $|n_{\mathbf{Q}}|$  show oscillatory decay towards a suppressed long time value. (ii) For  $E_0 \rightarrow E_0^c$ , these indicators first show a drop towards zero over a timescale of few phonon oscillations, remains small for a time  $\tau_{cr}$ , and then rise towards a finite steady state value. (iii) For  $E_0 > E_0^c$ , the indicators decay monotonically to zero.

(3). *‘Critical’ slowing down*: For  $E_0 \rightarrow E_0^c$  from below,  $|x_{\mathbf{Q}}(t \rightarrow \infty)|^2$  and  $|n_{\mathbf{Q}}(t \rightarrow \infty)|^2$  vanish as  $(E_0^c - E_0)^\alpha$  where  $\alpha \sim 0.7$ . We find that  $\tau_{cr}$  diverge as  $(E_0^c - E_0)^{-\nu}$ , where  $\nu \sim 0.45$ .

(4). *Time dependent spectrum*: Constructing a density of states (DOS) from the instantaneous eigenvalues we find that

the DOS remains gapped at all times when  $E_0 \ll E_0^c$ , and ungapped at all times for  $E_0 > E_0^c$ . For  $E_0 \rightarrow E_0^c$  the DOS first shows gap closing and then reopening as a function of time.

(5). *Phenomenology*: The coupled dynamics of electrons and phonons can be approximated by the dynamics of the phonons in the presence of a force arising from a *nonequilibrium* electron population. Parametrising this population distribution based on the full dynamics and using a Langevin equation allows us to capture both the suppression-revival dynamics as well as the ‘‘critical behaviour’’.

This paper is organised as follows. In Section II we define the model, explain the dynamical scheme, and set out the parameter space. In Section III we describe the classification of order parameter response into three regimes. Section IV provides a detailed characterisation of the order parameter response in terms of a few parameters. In Section V we examine the dynamics of the overall system, including the time dependence of the energy distribution over momentum modes, the electronic density of states, and the population of ‘excited’ electrons. Based on these we construct an effective classical model for the phonon dynamics in Section VI, allowing access to large spatial scales and long times. Section VII discusses issues related to our analytic and numerical approximations and Section VIII concludes the paper.

## II. MODEL AND METHOD

### A. Model and evolution equation

The Holstein model is given by:

$$\begin{aligned} H &= H_e + H_{ph} + H_{ep} \\ &= \sum_{ij} t_{ij} \hat{c}_i^\dagger \hat{c}_j + \sum_i \left( \frac{\hat{p}_i^2}{2M} + \frac{K \hat{x}_i^2}{2} \right) - g \sum_i \hat{n}_i \hat{x}_i \end{aligned}$$

For the  $t_{ij}$  we consider nearest neighbour hopping on a square lattice. We start by writing the Heisenberg equation for  $\hat{x}_i$ , leading to the family below. Setting  $\hbar = 1$ ,

$$\begin{aligned} \frac{d\hat{x}_i}{dt} &= -i[\hat{x}_i, H] = \frac{\hat{p}_i}{m} \\ \frac{d\hat{p}_i}{dt} &= -i[\hat{p}_i, H] = -K\hat{x}_i + g\hat{n}_i \end{aligned}$$

Now there are different options. (i) One can take an average on the left and right hand side of the equations and replace  $\langle \hat{n}_i(t) \rangle$  by its expectation in the instantaneous phonon background  $x_i(t)$ . This is the ‘adiabatic evolution’ (AE) scheme, and involves iterative diagonalisation of the electron problem in ‘classical’ phonon backgrounds  $\{x_i\}$  to compute the force on the phonons. Alternately, (ii) one can go beyond the adiabatic scheme and write an equation of motion for the  $\hat{n}_i(t)$  itself, and so on, and close the hierarchy at some order. Following this route:

$$\frac{d\hat{n}_i}{dt} = -i[\hat{n}_i, H] = -i \sum_{mn} t_{mn} [c_i^\dagger c_i, c_m^\dagger c_n]$$

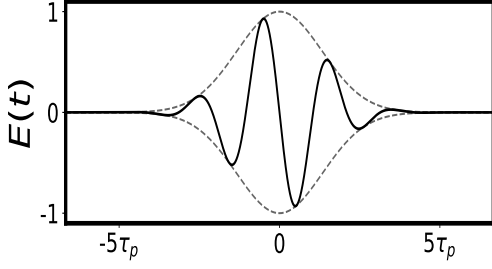


FIG. 1. Laser pulse: We set the pulse width to  $\tau_p = \tau_0/10$ , the pulse frequency  $\Omega_p = 5\Omega_0$ , and vary the magnitude of the electric field  $E_0$  from 0.01 – 1. We plot the time dependence of the electric field, normalized by  $E_0$ .

$$= -i \sum_{\alpha} t_{i\alpha} (c_{\alpha}^{\dagger} c_i - c_i^{\dagger} c_{\alpha}) = \sum_{\alpha} \hat{J}_{i\alpha}$$

$$\frac{d\hat{J}_{i\alpha}}{dt} = -i \sum_{mn} t_{mn} [\hat{J}_{i\alpha}, c_m^{\dagger} c_n] - ig \sum_j \hat{x}_j [\hat{J}_{i\alpha}, c_j^{\dagger} c_j]$$

Using  $[c_{\alpha}^{\dagger} c_{\beta}, c_m^{\dagger} c_n] = \delta_{n\alpha} c_m^{\dagger} c_{\beta} - \delta_{m\beta} c_{\alpha}^{\dagger} c_n$  and simplifying the commutators, we obtain:

$$\frac{d\hat{J}_{i\alpha}}{dt} = -t_{i\alpha} \sum_{mn} t_{mn} \hat{f}_{mn}^{i\alpha} - gt_{i\alpha} \sum_j \hat{x}_j \hat{h}_j^{i\alpha}$$

where the  $f$  and  $h$  are fermion bilinears. The first term comes purely from the hopping, the second term however involves a cross coupling between electron and phonon variables. The equations are not closed and now we need to know the dynamics of mixed objects like  $\hat{x}_j \hat{h}_j^{i\alpha}$ , etc. This leads to the Bogoliubov-Born-Green-Kirkwood-Yvon (BBGKY) hierarchy. We truncate the hierarchy by taking the expectation value of the LHS and RHS and approximating:  $\langle \hat{x}_j \hat{h}_j^{i\alpha} \rangle \approx \langle \hat{x}_j \rangle \langle \hat{h}_j^{i\alpha} \rangle$ . The factorisation leads to a closed family of equations. This ‘non adiabatic evolution’ (NAE) scheme involves two processes: (i) The phonons are ‘driven’ by  $-Kx_i + gn_i$ , with  $n_i = \rho_{ii}$ , where  $\rho$  is the one body ‘density operator’, and (ii) the density operator  $\rho_{ij}$  is non locally correlated and driven by the  $x_j$ .

Instead of writing a two step equation for  $n_i$  and current we could have directly written an equation for  $\rho_{ij}$ , factorised it as above, and used the local component  $\rho_{ii}$  in the phonon equation. The coupled equations would be:

$$m \frac{d^2 \hat{x}_i}{dt^2} = -K \hat{x}_i + g \hat{\rho}_{ii}$$

$$\frac{d\hat{\rho}_{ij}}{dt} = -i[\hat{\rho}_{ij}, \tilde{H}] = -i([\hat{\rho}_{ij}, H_e] + [\hat{\rho}_{ij}, H_{ep}])$$

$$= -i[\hat{\rho}_{ij}, H_e] + ig \sum_m [\hat{\rho}_{ij}, \hat{n}_m] \hat{x}_m$$

We take the expectation value of both sides and factorise.

## B. Generating the initial configuration

We consider the equilibrium system to be in its ground state. At half filling,  $n = 0.5$ , the Holstein model with nearest neighbour hopping has a charge ordered ground state at all  $g$ . The CO is driven by a Fermi surface instability at small  $g$  and the virtual hopping of polarons at large  $g$ . We obtain the reference CO state by minimising the total energy with respect to a periodic  $x_i$  field. At the minimum,  $\{x_i^0\}$ , say, we use the the eigenvectors of  $H\{x_i^0\}$  to compute the averages  $\rho_{ij}^0 = \langle c_i^{\dagger} c_j \rangle_0$ .

## C. Modeling the laser pulse

We include the laser field via Peierls substitution. This leads to the time dependent hopping term:

$$H_e(t) = \sum_{ij} t_{ij} (e^{i \int_{r_j}^{r_i} \vec{A}(t) \cdot d\vec{r}} c_i^{\dagger} c_j + h.c)$$

$$\vec{E}(t) = -\frac{d\vec{A}(t)}{dt} = E_0 \exp[-(\frac{t-t_0}{\tau_p})^2] \cos(\Omega_p t)$$

$E_0$  is the strength of the field,  $\tau_p$  and the  $\Omega_p$  are the width of the pulse and frequency of the incident wave respectively. The electric field is taken in  $(\vec{x} + \vec{y})$  direction. We set  $t_0 = 0$ . The time dependence of the electric field associated with the laser pulse is shown in Fig.1.

## D. Parameter space

In the rest of the paper we will use  $t$  as the time variable and denote the hopping  $t_{ij}$  as  $-t_{hop}$  for nearest neighbours, and set  $t_{hop} = 1$ . We set  $K = 1$  and the oscillator mass to  $M = 25$  so that the local phonon frequency is

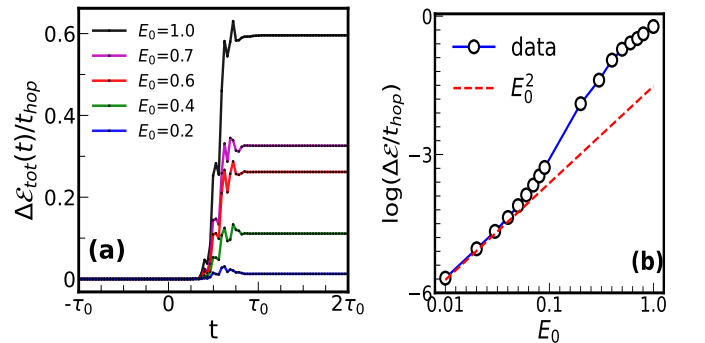


FIG. 2. (a) The time dependence of the change in the total energy  $\Delta\mathcal{E}(t)$ . The energy of the unperturbed system is  $\mathcal{E}(0)$  and pumping injects an amount of energy  $\Delta\mathcal{E}$ . Since the post pulse dynamics is conservative, total energy  $\mathcal{E}_{tot}(t) = \mathcal{E}(0) + \Delta\mathcal{E}(t)$  should be constant for  $t \gg \tau_p$ . The panel confirms this and also quantifies  $\Delta\mathcal{E}(E_0)$ . (b). The dependence of  $\Delta\mathcal{E}$  on  $E_0$ , showing the ‘linear response’ regime,  $\Delta\mathcal{E} \propto E_0^2$ , and beyond.

$\Omega_0 = \sqrt{K/M} = 0.2$ . As a result the ‘‘adiabaticity’’ parameter  $\gamma = \Omega_0/t_{hop} = 0.2$ , small but not negligible. We measure time in units of  $\tau_0 = 2\pi/\Omega_0$ . We focus on the half-filled case  $n = 0.5$ . In the adiabatic regime the energy of a polaron is  $E_p \sim -g^2/2K$ . A polaron forms when this equals the band bottom energy  $-4t_{hop}$  (in two dimensions). This leads to the definition of a dimensionless EP coupling strength:  $\lambda = g^2/8Kt_{hop}$ . Single polaron formation, in the adiabatic limit, corresponds to  $\lambda \sim 1$ . In the paper we work mainly with  $\lambda = 0.38$ , intermediate coupling but well below the single polaron threshold. We set  $\Omega_p/\Omega_0 = 5$  and  $\tau_p = \tau_0/10$ . Having fixed  $n$ ,  $t_{hop}$ ,  $\Omega_0$ ,  $\lambda$ , and the pulse parameters  $\tau_p$  and  $\Omega_p$ , we study the response of the half filled CO state to a laser pulse for varying pulse amplitude  $E_0$ .

### E. Numerical techniques

Most of our data are on system size  $N = 16 \times 16$ . We use the Runge-Kutta 4 (RK4) method to solve  $N^2 + 2N$  coupled first order differential equations for  $x_i$ ,  $p_i$  and  $\rho_{ij}$ . Our step parameter is set to  $\delta t = \tau_0/1500$  our total run length  $\tau_{max}$  is at least  $6000\tau_0$ . In the critical pulse regime, where the system undergoes a transition from the CO state to a charge disordered state, simulation timescales needed to access the steady state grow rapidly. There we have used  $\tau_{max} \sim 10^5\tau_0$  (on system size  $12 \times 12$ ).

### F. Indicators

Our basic output is the time series for  $x_i(t)$ . Based on this we can compute various correlation functions of the phonon variables. We can compute the instantaneous electronic density of states (DOS) from the electronic eigenvalues  $\epsilon_n$  in a background  $x_i(t)$ . We also have access to the equal time correlation  $\rho_{ij}(t) = \langle c_i^\dagger(t)c_j(t) \rangle$  and can compute the ‘occupation’ of levels  $\epsilon_n(t)$  from this. The spatial Fourier transforms related to phonon distortions and density are, respectively:

$$x_{\mathbf{q}}(t) = \frac{1}{N} \sum_{ij} e^{i\mathbf{q}\cdot\mathbf{r}_i} x_i(t), \quad n_{\mathbf{q}}(t) = \frac{1}{N} \sum_{ij} e^{i\mathbf{q}\cdot\mathbf{r}_i} n_i(t)$$

where  $n_i(t) = \rho_{ii}(t)$ . There are the corresponding Fourier transforms to frequency:  $x_{\mathbf{q}}(\omega) = \int_0^{\tau_{max}} dt e^{-i\omega t} x_{\mathbf{q}}(t)$ . We also calculate the following instantaneous distributions

$$N(\omega, t) = \frac{1}{N} \sum_n \delta(\omega - \epsilon_n(t)), \quad P(x, t) = \frac{1}{N} \sum_i \delta(x - x_i(t))$$

The occupation function  $f(\omega, t)$  for the instantaneous eigenstates is defined by:

$$f(\omega, t)N(\omega, t) = \sum_n \rho_{nn}(t)\delta(\omega - \epsilon_n(t))$$

Where the  $\rho_{nn}$  is the expectation value of the density operator associated with the  $n$ -th eigenstate with energy  $\epsilon_n$ :  $\rho_{nn}(t) = \sum_{ij} U_{in}^*(t)U_{jn}(t)\rho_{ij}(t)$ , where  $U(t)$  are the instantaneous eigenvectors.

## III. GLOBAL BEHAVIOUR OF ORDER PARAMETER

Before entering into the detailed characterisation of the dynamics we attempt a broad classification of regimes that occur for varying  $E_0$ . In the absence of an external drive our method of evolution strictly conserves the energy. If the pre-pulse energy of the system is  $\mathcal{E}(0)$  and the pump adds an energy  $\Delta\mathcal{E}$  then the energy  $\mathcal{E}(t)$  for  $t \gg \tau_p$  is  $\mathcal{E}_{final} = \mathcal{E}(0) + \Delta\mathcal{E}(E_0)$  independent of time. In Fig.2(a) we depict the time evolution of  $\mathcal{E}(t)$  with varying strength  $E_0$ . Fig.2(b) shows  $\Delta\mathcal{E}$  against  $E_0$ , revealing that at low  $E_0$ , it is proportional to  $\sim E_0^2$  as expected from linear response.

Fig.3 illustrates the different dynamical regimes that arise in response to pulses of increasing strength. The data is for  $\lambda = 0.38$ , the results have a similar trend at other  $\lambda$ . The charge ordered state corresponds to  $O(1)$  value of the Fourier transform  $x_{\mathbf{Q}} = (1/N) \sum_i x_i e^{i\mathbf{Q}\cdot\mathbf{r}_i}$ , the order parameter of the CO state. The upper row in Fig.3 shows the time dependence of  $|x_{\mathbf{Q}}(t)|$ . The pre-pulse value is normalised to 1 for convenience. Panels (a)-(b) are in the ‘weak pulse’ regime where we mainly see oscillatory decay to a long time value that is suppressed with respect to the pre-pulse (equilibrium) value. We will call this response ‘‘weak oscillatory suppression’’ (WOS). Panel (c) show results in the ‘critical pulse’ regime where  $|x_{\mathbf{Q}}(t)|$  initially drops almost to zero, stays there for some time, and then ‘revives’ heading towards a finite long time value. We call this ‘‘strong suppression and revival’’ (SSR) dynamics. Panel (d) shows  $|x_{\mathbf{Q}}(t)|$  in the strong pulse regime where we see a monotonic decay of the oscillation envelop to zero and there is no revival. This is simply ‘‘monotonic suppression’’ (MS) dynamics.

The lower row in Fig.3 shows the time Fourier transform of the corresponding upper panels, taken over the interval  $0 - 6000\tau_0$ . The character of  $|x_{\mathbf{Q}}(\omega)|^2$  can be understood from the behaviour of  $x_{\mathbf{Q}}(t)$ .

When the energy added by the pulse is very small as in (e)-(f) it leads to weakly damped oscillation of the various normal modes of the CO state. The oscillation frequency would be  $\Omega_{\mathbf{Q}}^0$ , the electronically renormalised phonon dispersion about the CO state (discussed later). The amplitude of oscillation of the modes will depend on the specific nature of the perturbation. The order parameter mode will have a response of the form  $x_{\mathbf{Q}} \sim A + B\cos(\Omega_{\mathbf{Q}}^0 t)$ . The lineshape will have a sharp feature at  $\Omega_{\mathbf{Q}}^0$  as observed in (e). With growing excitation mode coupling leads to a damping, as seen in (b), and  $x_{\mathbf{Q}} \sim A + Be^{-t/\tau_w}\cos(\Omega_{\mathbf{Q}} t)$ . We denote the decay time in the weak pulse regime as  $\tau_w$ , and  $\Omega_{\mathbf{Q}}$  is the oscillation frequency now renormalised by  $E_0$ . The damping rate  $\Gamma_w = \tau_w^{-1}$  increases with  $E_0$ . However,  $\tau_w \gg \tau_0$  so the damping  $\Gamma_w \ll \Omega_{\mathbf{Q}} \sim \Omega_0$ .

For pulse strength in the critical window the general feature of  $x_{\mathbf{Q}}(t)$  is rapid suppression at small times, a seeming quiescent period, and then a revival. The behaviour is accompanied by weak oscillation about the mean curve. Ignoring the sharp drop at small times, the longer time behaviour can be described roughly by  $x_{\mathbf{Q}}(t) \sim Ae^{-(\tau_{cr}/t)^\beta} + B\cos(\Omega_{\mathbf{Q}} t)$ . The ‘waiting time’ in the low amplitude state is decided by  $\sim \tau_{cr}$ , while the approach to the long time state has a power

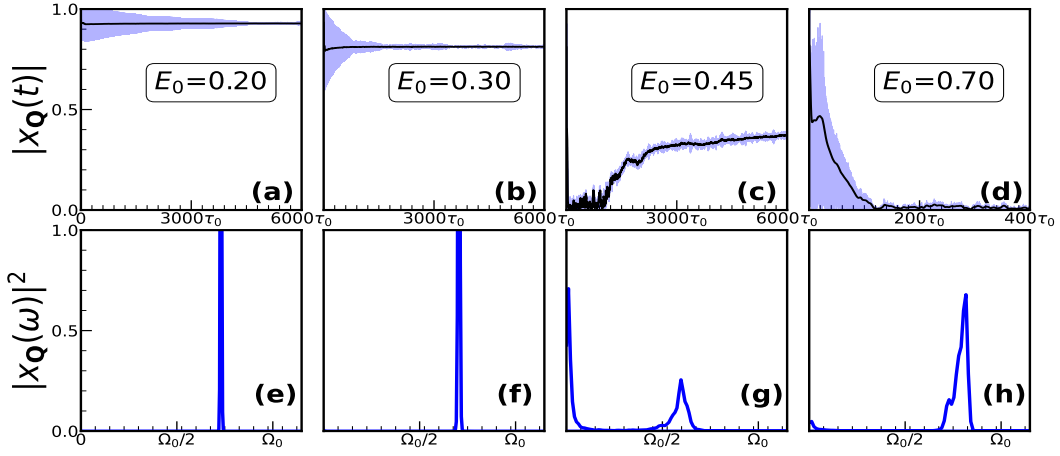


FIG. 3. Overview of dynamics of the order parameter mode  $|x_{\mathbf{Q}}|$  for different  $E_0$ . Upper row: panels (a)-(d) show real time dynamics:  $|x_{\mathbf{Q}}(t)|$ . (a)-(b) Weak pulse regime, roughly  $E_0 = 0 - 0.35$ , where  $x_{\mathbf{Q}}(t)$  oscillates with a single frequency and decays to a suppressed CO state. (c) Critical pulse regime, roughly  $E_0 = 0.35 - 0.50$ , where  $x_{\mathbf{Q}}(t)$  is rapidly suppressed, stays small for a time window, and then rises to a low amplitude long time state. (d) Strong pulse regime:  $E_0 > 0.5$ , where the CO gets destroyed within a few  $\tau_0$  while the phonon ringing continues for a longer time. Lower row:  $|x_{\mathbf{Q}}(\omega)|^2$ , where  $x_{\mathbf{Q}}(\omega)$  is the Fourier transform of  $x_{\mathbf{Q}}(t)$  over the whole time window. (e)-(f) The weak pulse  $|x_{\mathbf{Q}}(\omega)|^2$  has primary feature at the electronically renormalised phonon frequency  $\Omega_{\mathbf{Q}}$ . There is a small broadening of the lines due to mode coupling induced decay. (g) In the critical pulse regime the spectrum has a broad feature at finite frequency and another feature around  $\omega = 0$ . (h) Spectrum in the strong pulse window, where the real time behaviour is oscillatory decay. System size  $16 \times 16$ .

law character  $1 - (\tau_{cr}/t)^\beta$ . The Fourier transform, panel (g), involves a low energy feature of width  $\sim (\tau_{max} - \tau_{cr})^{-1}$  and a broadened line around  $\Omega_{\mathbf{Q}}$ .

In (h), the strong pulse regime, there is a stable oscillation amplitude at short times followed by a monotonic decay to zero. A simple analytic form for  $x_{\mathbf{Q}}(t)$  is  $A(1 - e^{-(\tau_s/t)^\gamma})\cos(\Omega_{\mathbf{Q}}t)$ . The low frequency feature quickly vanishes as  $E_0$  increases in this regime.

We collect together the expressions for  $x_{\mathbf{Q}}(t)$ :

$$\begin{aligned} x_{\mathbf{Q}}(t) &\sim A + Be^{-t/\tau_w} \cos(\Omega_{\mathbf{Q}}t) && \text{(weak)} \\ &\sim Ae^{-(\tau_{cr}/t)^\beta} + B\cos(\Omega_{\mathbf{Q}}t) && \text{(critical)} \\ &\sim A(1 - e^{-(\tau_s/t)^\gamma})\cos(\Omega_{\mathbf{Q}}t) && \text{(strong)} \end{aligned}$$

Fig.4(a) shows the global phase diagram in the  $\lambda - E_0$  plane, highlighting both the long time state and the dynamical regimes. It is based on analysis of the kind shown in Fig.3, now carried out for several  $\lambda$ . The blue region corresponds to surviving CO, while the red region corresponds to a state with CO destroyed in response to the pulse. In the ordered region, dark blue (WOS) corresponds to the weak oscillatory suppression defined earlier, while light blue (SSR) corresponds to strong suppression and revival. Red region (MS) is charge disordered, where the dynamics is of monotonic suppression, and is separated from the ordered regime by the nonequilibrium phase transition. A true phase transition, with  $|x_{\mathbf{Q}}(t \rightarrow \infty)| \rightarrow 0$ , as  $E_0$  tends to some  $E_0^c$ , can be seen only as  $L \rightarrow \infty$  and  $t_{max} \rightarrow \infty$ . The boundary in Fig.4(a) is drawn via extrapolation of  $L$  dependent data at a few sizes,  $12 \times 12$  to  $20 \times 20$ .

Fig.4(b) shows the phase diagram in terms of  $\lambda$  and the energy absorbed. We make a rough estimate of the transition line

(dotted) using a electronic temperature model introduced later (Section VI). Briefly, the excess energy  $\Delta\mathcal{E}$  associated with population transfer to the upper-level destroys the double well structure in  $x_{\mathbf{Q}}$  at  $\Delta\mathcal{E} \sim \Delta\mathcal{E}_c$ . We estimate this value in the following way: We assume a finite electronic temperature  $T_{el}$  and using a uniform distortion in  $\mathbf{Q}$ -mode we calculate the effective potential by evaluating the eigen values  $\epsilon_n$ ,

$$V_{eff}(x_{\mathbf{Q}}, T_{el}) = \frac{1}{N} \sum_n \epsilon_n F(\epsilon, T_{el}) + \frac{1}{2} K x_{\mathbf{Q}}^2$$

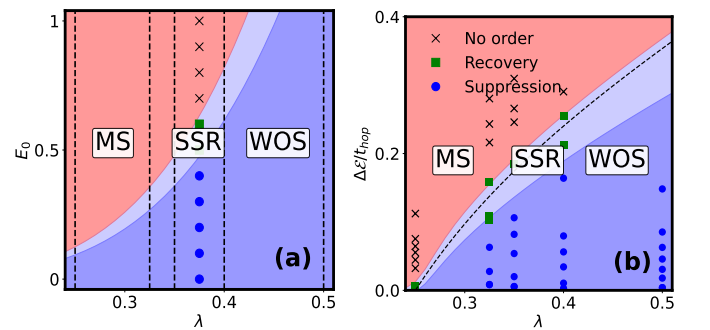


FIG. 4. (a)  $\lambda - E_0$  global phase diagram in terms of the long time state and the dynamics that arises in response to a pulse. In the blue regions the long time state has charge order. In dark blue,  $|x_{\mathbf{Q}}|$  shows an oscillatory decay towards its long time CO state. In region light blue,  $|x_{\mathbf{Q}}|$  shows an initial decay to zero and then revives towards a low amplitude CO state at long times. In red region,  $|x_{\mathbf{Q}}|$  shows monotonic decay to zero with no revival. The boundary between regions blue and red is a phase transition. (b) Phase diagram in terms of energy absorbed,  $\Delta\mathcal{E}$ . The dotted line, based on high electronic temperature calculation (see text), roughly captures the transition line.

$F(\epsilon, T_{el})$  being the Fermi function. This loses its double well structure at  $T_{el} \sim T_{el}^c$  and at  $T_{el}^c$  we calculate the change in energy as  $\Delta\mathcal{E}_c = \min(V_{eff}(x_{\mathbf{Q}}, T_{el}) - \min(V_{eff}(x_{\mathbf{Q}}, 0)))$ . This shows if the system absorbs energy  $\Delta\mathcal{E} < \Delta\mathcal{E}_c$  the long time state shows a finite  $|x_{\mathbf{Q}}|$ .

#### IV. DETAILED DYNAMICS OF ORDER PARAMETER

##### A. Weak pulse regime

Fig.5 shows in detail the phonon and charge density dynamics at the ordering wavevector  $\mathbf{Q}$  for a weak pulse,  $E_0 = 0.30$ . For both the phonon and the density field there is an initial drop, on the scale of a few  $\tau_0$ . This is followed by an oscillatory decay to a long time state. Panels (a) and (c) show  $|x_{\mathbf{Q}}|$  and  $|n_{\mathbf{Q}}|$ , respectively, over the whole run, while the insets show the time dependence at short times  $\sim 15\tau_0$ . As we have argued,  $x_{\mathbf{Q}}(t) \sim A + B e^{-t/\tau_w} \cos(\Omega_{\mathbf{Q}} t)$ . This simple function does not capture the oscillations (and the ‘beating pattern’) at  $t \gg \tau_w$  but seems adequate for an overall description. Also, to capture the  $t = 0$  state we should have  $A + B = 1$ . Panels (b) and (d) show the respective Fourier transforms, the main panel showing the transform of the full time series and the inset showing the transform of the short time response.

In Fig.6 panel (a) shows the fit to the  $|x_{\mathbf{Q}}|$  envelop using the fitting function above. According to the fitting function, the  $t \rightarrow \infty$  value of  $|x_{\mathbf{Q}}|$  is  $A$  and there will be a peak in the spectrum around  $\Omega_{\mathbf{Q}}$  with width  $\tau_w^{-1}$ . Panel (b) shows the  $E_0$  dependence of  $A$  and  $B$ .  $A$  falls from 1 at  $E_0 = 0$  to  $\sim 0.6$  at  $E_0 \sim 0.35$  while  $B$  rises from zero to about 0.4.

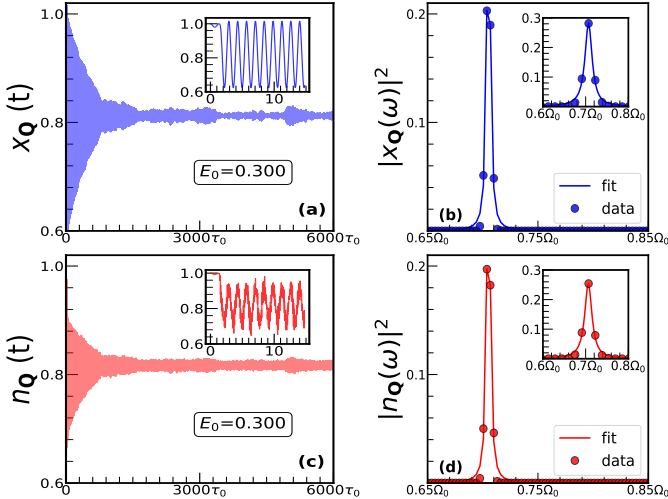


FIG. 5. Weak pulse regime: (a) shows  $|x_{\mathbf{Q}}(t)|$  with the inset highlighting the very short time behaviour. (b) Shows  $|x_{\mathbf{Q}}(\omega)|^2$ , obtained by Fourier transform over the entire time window, while the inset shows the transform of data over the interval  $t \sim [0 - 15]\tau_0$ . (c) and (d) show corresponding data for  $|n_{\mathbf{Q}}(t)|$  and  $|n_{\mathbf{Q}}(\omega)|^2$ . Note the quick drop in  $|n_{\mathbf{Q}}(t)|$  at very short time. During this time, the electron dynamics is primarily governed by the pump, and the density modulation can reduce despite the presence of a lattice distortion.

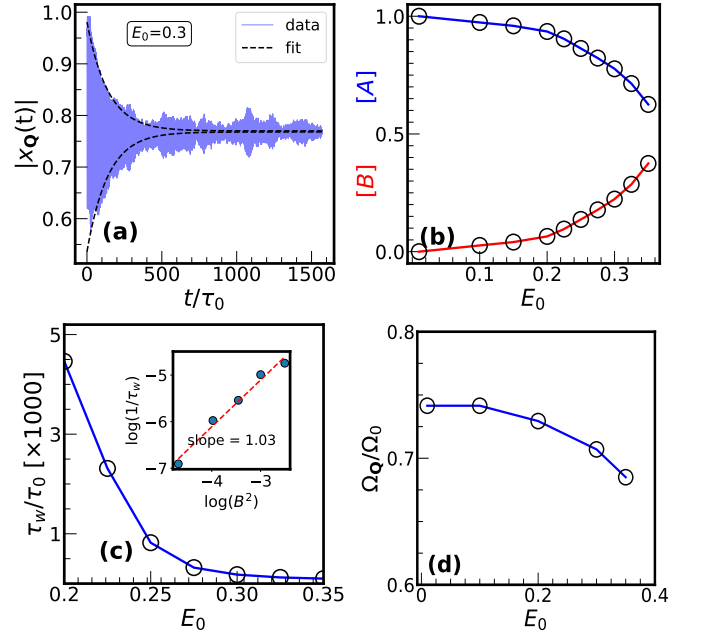


FIG. 6. Characterising dynamics in the weak pulse regime. We fit the  $|x_{\mathbf{Q}}(t)|$  to the form given in the text. (a) Shows the fit to the envelop. (b) Shows the amplitude  $A(E_0)$ , with  $A$  being the steady state value of  $|x_{\mathbf{Q}}(t)|$  at the ordering wave vector  $\mathbf{Q}$ . Note the sharp downward trend already apparent at  $E_0 \sim 0.35$ . (c) Shows the timescale  $\tau_w$  over which the main oscillations decay. It diverges as  $E_0 \rightarrow 0$  when the dynamics reduces to decoupled normal modes. In the inset we plot  $\log(B^2)$  with  $\log(\tau_w^{-1})$  and it shows a slope  $\sim 1.03$  showing the relationship  $\tau_w^{-1} \sim 1/B^2$ . (d) Shows the oscillation frequency  $\Omega_{\mathbf{Q}}$  which shows a downward trend, akin to what one observes on raising temperature.  $\Omega_{\mathbf{Q}}$  has electronic renormalisation effects built into it even at  $E_0 = 0$ .

Panel (c) shows  $\tau_w(E_0)$ , which has a remarkable decrease with increasing  $E_0$ . As  $E_0 \rightarrow 0$  the weakly perturbed lattice has only undamped normal mode oscillations, and  $\tau_w \rightarrow \infty$ . Since  $\tau_w^{-1}$  emerges from anharmonicity, in the weak pulse limit we expect it to vary as a power  $B^\alpha$ . A plot of  $\log(B)$  versus  $\log(\tau_w^{-1})$  suggests that  $\tau_w^{-1} \sim B^2$ .

The oscillation frequency,  $\Omega_{\mathbf{Q}}$ , shows only weak  $E_0$  dependence. The frequency for low amplitude oscillations on the CO state is given by  $\Omega_{\mathbf{Q}} = \sqrt{\Omega_0^2 + (g^2/m)\Pi_{\mathbf{Q}}^0}$ , where  $\Pi_{\mathbf{Q}}^0$  is the density response function of the CO state at momentum  $\mathbf{Q}$  [52]. Electron-phonon coupling gives a dispersion to the phonons, and also lowers the frequency from the bare value  $\Omega_0$ . The effect of the added energy due to  $E_0$  is to additionally reduce  $\Omega_{\mathbf{Q}}$ , akin to what one observes in the effect of temperature [53].

##### B. Critical pulse strength regime

For  $E_0 \gtrsim 0.35$  the nature of  $|x_{\mathbf{Q}}(t)|$  changes. Beyond a few cycles of oscillatory response both the phonon and charge density fields are suppressed to roughly  $\sim 1 - 2\%$  of their pre-pulse value, and persist in this state - with small oscil-

lations - for a timescale that we call  $\tau_{cr}$ . Beyond this both  $|x_{\mathbf{Q}}(t)|$  and  $|n_{\mathbf{Q}}(t)|$  ‘revive’, reaching a finite but low amplitude long time state. Fig.7.(a) and (c) show the time dependence of the two structure factors at  $E_0 = 0.45$ , the main panels show the overall time dependence while the inset shows the initial drop that occurs over  $\sim 25\tau_0$ . A description of the form  $x_{\mathbf{Q}}(t) \sim Ae^{-(\tau_{cr}/t)^\beta} + B\cos(\Omega_{\mathbf{Q}}t)$  captures multiple features of the complex dynamics. Beyond the initial drop the function above captures the following features of the data: (i) The low amplitude quiescent state, at  $t \lesssim \tau_{cr}$ , is described by exponentially small contribution from the first term, and small oscillations  $B|\cos(\Omega_{\mathbf{Q}}t)|$ , with  $B \ll 1$ . (ii) As  $t$  goes beyond  $\tau_{cr}$  the  $A$  term makes a significant contribution, seen in the rise of the mean curve. The exponential saturates for  $t \gg \tau_{cr}$  but long term oscillations persist. (iii) Finally, the mean value of  $|x_{\mathbf{Q}}|$  rises as  $1 - (\tau_{cr}/t)^\beta$  at long times, a power law rather than exponential rise to the steady state.

Panels (b) and (d) show  $|x_{\mathbf{Q}}(\omega)|$  and  $|n_{\mathbf{Q}}(\omega)|$ , respectively. There are the usual features around  $\Omega_{\mathbf{Q}}$  There is also an interesting low energy feature, whose width is  $\sim (\tau_{max} - \tau_{cr})^{-1}$ .

Fig.8 panel (a) compares the actual data to a fit of the form assumed. We have shown only the envelop since showing the oscillations is not feasible over  $6000\tau_0$ . As we have stated the single scale  $\tau_{cr}$  describes both the low amplitude quiescent state as well as the power law rise to the steady state. Panel (b) shows the amplitude  $A(E_0)$ . In a later figure we will show the size dependence of this result, allowing us to extract the critical behaviour. (c) shows the rapid rise of the ‘delay time’  $\tau_{cr}$  that is needed for revival of the CO state. (d) Shows the exponent  $\beta$  that controls the power law approach to the steady state. (e) and (f) show the amplitude  $B$ , controlling the oscill-

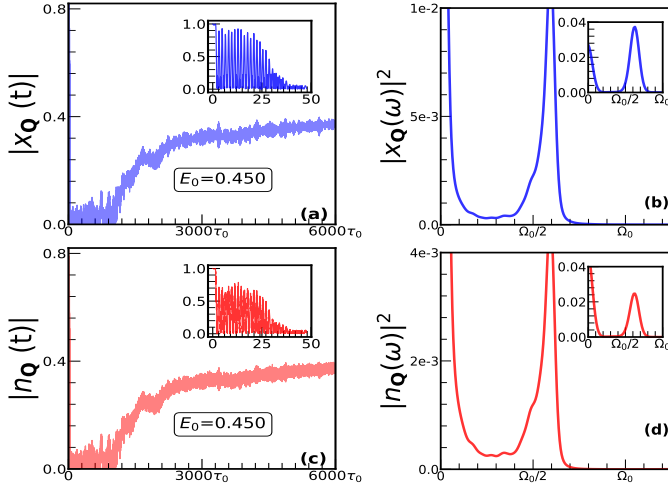


FIG. 7. Critical pulse strength regime: (a) and (c) shows real time behaviour of  $|x_{\mathbf{Q}}(t)|$  for the phonons and the electron density, respectively. Corresponding insets show the behaviour at short times,  $t \lesssim 50\tau_0$ . At short time the ordering amplitude in both phonons and electrons decay to zero. Then there is a very low amplitude quiescent state, followed by a ‘revival’ - rising to the long time value as  $|x_{\mathbf{Q}}(t)| \sim e^{-(\tau/t)^\beta}$ . The respective lineshapes, (b) and (d), show a peak near zero as well as broad finite frequency feature at  $\Omega_{\mathbf{Q}}$ .

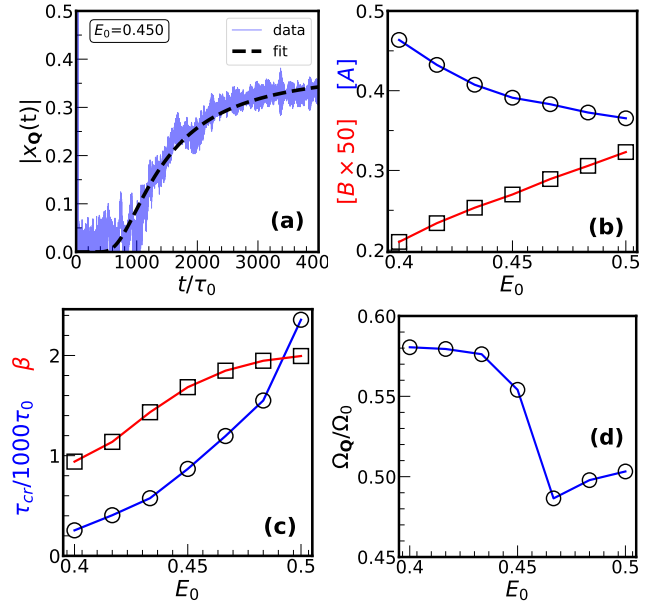


FIG. 8. Characterising dynamics in the critical pulse regime. We fit  $x_{\mathbf{Q}}(t)$  to the form  $Ae^{-(\tau_{cr}/t)^\beta} + B\cos(\Omega_{\mathbf{Q}}t)$ . (a) Comparison of the growth part  $Ae^{-(\tau_{cr}/t)^\beta}$  of the fit function with the actual data at  $E_0 = 0.45$ . (b) The amplitude  $A$  (blue) that decides the steady state value of  $|x_{\mathbf{Q}}|$  and  $B$  (red) that decides the size of oscillations. Note that  $B$  is one order of magnitude smaller than  $A$  for the system size we have studied here. (c) The increase in  $\tau_{cr}$  (blue) by more than an order of magnitude while  $E_0$  varies only from 0.41 to 0.47, and the exponent  $\beta$  (red) which stays between 0 – 1. (d) The frequency  $\Omega_{\mathbf{Q}}$  shows non-monotonic behaviour, dropping and then rising with increasing  $E_0$ .

lations, and the primary frequency  $\Omega_{\mathbf{Q}}$ .

### C. Strong pulse regime

Fig.9 shows the detailed dynamics at  $E_0 = 1.0$ , which is in the strong pulse regime. Panel (a) shows  $|x_{\mathbf{Q}}(t)|$ , it has a modest drop on the scale of  $\tau_0$ , then a period of roughly constant amplitude oscillation for about  $25\tau_0$ , and finally a decay to zero that seems to be fit by a power law. For our fitting function:  $x_{\mathbf{Q}}(t) \sim A(1 - e^{-(\tau_s/t)^\gamma})\cos(\Omega_{\mathbf{Q}}t)$ , the  $t \ll \tau_s$  regime is of fixed amplitude oscillation,  $|A\cos(\Omega_{\mathbf{Q}}t)|$  while for  $t \gg \tau_s$  we get a behaviour  $|A(\tau_s/t)^\gamma\cos(\Omega_{\mathbf{Q}}t)|$ .

The response in the charge sector, panel (c), is very different.  $|n_{\mathbf{Q}}|$  falls sharply from 1 to  $\sim 0.15$  within  $t \sim \tau_0$ , then has roughly fixed amplitude oscillations for  $t \lesssim \tau_s$ , and then abruptly collapses. We do not see any prominent power law tail (at least at this value of  $E_0$ ) unlike in  $|x_{\mathbf{Q}}|$ . Panels (b) and (d) show the corresponding Fourier transforms. Both of these have the usual peaks at  $\Omega_{\mathbf{Q}}$ .

Fig.10 shows the fit to the strong pulse data and the variation of the fit parameters with  $E_0$ . Panel (a) shows the fit to the actual data using the assumed functional form. Both the fixed amplitude part and the ‘power law’ decay in  $x_{\mathbf{Q}}$  are captured reasonably by the fit function. Panel (b) shows the timescale

$\tau_s$  which *increases* initially with increasing  $E_0$  (past  $E_0^c$ ) and then tends to saturate. Panel (c) shows the exponent  $\gamma$ , which reduces from  $\sim 2.5$  to  $\sim 1.5$  as  $E_0$  increases from 0.6 to 1.0. In (d)  $\Omega_{\mathbf{Q}}$  increases with  $E_0$  tending to the bare  $\Omega_0$  (independent local oscillators) at large  $E_0$ . The amplitude  $A$  is almost flat in this regime at  $A = 0.88$ .

## V. DYNAMICS OF THE OVERALL SYSTEM

Till now the focus has been on the order parameter mode at  $\mathbf{q} = (\pi, \pi) \equiv \mathbf{Q}$ . We now pay attention to the other  $\mathbf{q}$  modes to which energy is transferred from  $\mathbf{Q}$  via mode coupling, and also the electron population - which dictates the overall energy sharing between electrons and phonons.

### A. Dynamics of momentum modes

We first look at evolution of  $|x_{\mathbf{q}}(t)|^2$  over the Brillouin zone (BZ) for three representative values of pulse amplitude. We also examine  $|x_{\mathbf{q}}(\omega)|^2$ , obtained by Fourier transforming  $x_{\mathbf{q}}(t)$  over the whole time window, for scans across the BZ.

Our  $x_i(t)$  is ‘driven’ by the density variable  $n_i(t)$ . When the  $x_i$  and the corresponding density deviate only slightly from the ideal periodic value we obtain normal mode vibrations at frequencies given by:

$$\Omega_{\mathbf{q}} = \sqrt{\Omega_0^2 + (g^2/m)\Pi_0(\mathbf{q})}$$

where  $\Pi_0$  encodes the density response of the CO state to a change in  $x$ .

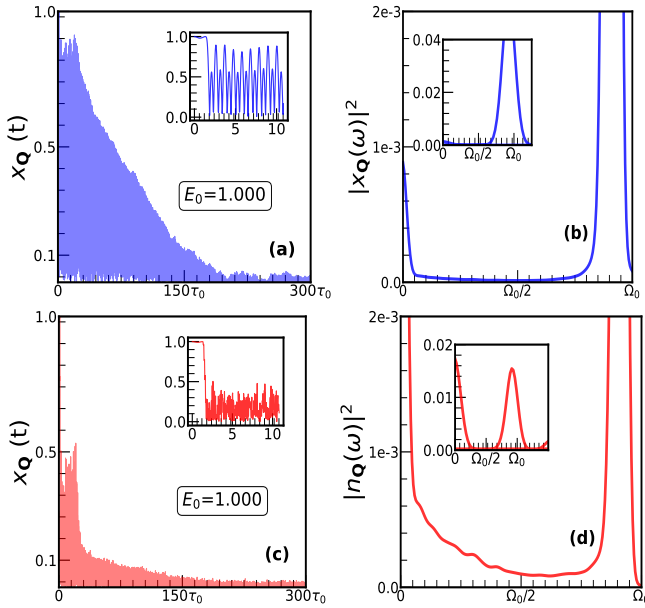


FIG. 9. Strong pulse regime: (a) The relatively slow decay of  $|x_{\mathbf{Q}}(t)|$  contrasted with (c) the rapid suppression of  $|n_{\mathbf{Q}}(t)|$ . (b) and (d) show the Fourier transforms of  $x_{\mathbf{Q}}(t)$  and  $n_{\mathbf{Q}}(t)$ , respectively.

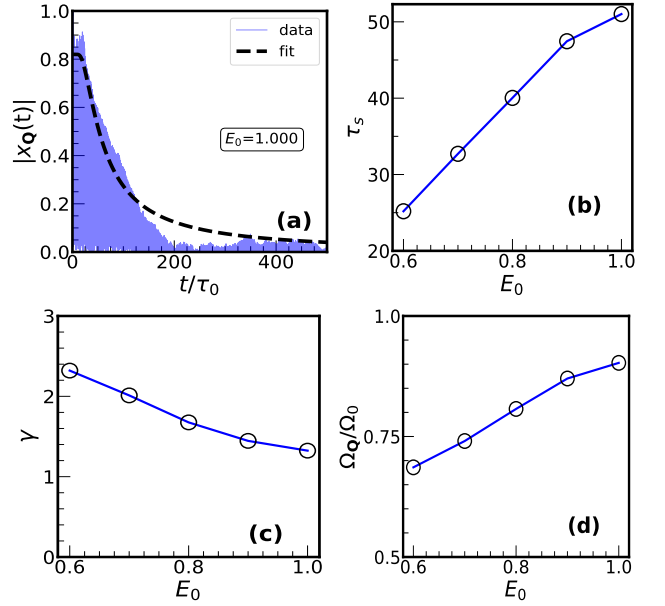


FIG. 10. Strong pulse regime: fit to  $|x_{\mathbf{Q}}(t)|$ , and fitting parameters. (a) Shows the fit to the envelop, capturing both the initial flat part and the longer term decay using the same timescale  $\tau_s$ . (b) and (c) Shows monotonic increase of  $\tau_s$  and decrease of the exponent  $\gamma$  with  $E_0$ . (d) Shows the increase in the oscillation frequency towards  $\Omega_0$  as  $E_0$  increases. We are not showing the amplitude  $A$ , which stays almost constant at  $A \sim 0.88$ .

This undamped oscillatory behavior is observed only at very weak pumping, as we have seen in Fig.3(a). It does not capture mode coupling, that leads to damping, or to the loss and revival phenomena that we observe in the critical regime. These effects involve the energy distribution over all  $\mathbf{q}$  as a function of time and also the nature of electronic excitations.

Fig.11 shows maps of  $|x_{\mathbf{q}}|$  at different times for three values of  $E_0$  and the associated  $|x_{\mathbf{q}}(\omega)|^2$ . In the left column, at  $t = 0$  (pre-pulse) and for all values of  $E_0$ , the only ‘bright’ feature is at  $\mathbf{q} = \mathbf{Q}$ . Other modes are inactive. The principal observations from the time dependence are the following:

(i) *Weak pulse regime (top row)*: At short time,  $\sim 50\tau_0$ , the first additional features show up along the diagonal of the Brillouin zone (BZ). The peak at  $\mathbf{Q}$  still remains the most prominent. At  $75\tau_0$  there are more excitations along the diagonal and by  $150\tau_0$  the whole BZ is ‘lit up’ the brightest part being along the diagonal. This is related to the nature of the pump, which is along  $\vec{x} + \vec{y}$  and causes an initial current in the  $\vec{x} + \vec{y}$  direction. The mode at  $\mathbf{Q}$  remains the most prominent at all times, diminishing slightly in intensity. The Fourier transform  $|x_{\mathbf{q}}(\omega)|^2$  essentially matches the phonon dispersion  $\Omega_{\mathbf{q}}$  of the charge ordered phase, but with the brightest intensity at  $\mathbf{q} = \mathbf{Q}$ . We are probing linear response.

(ii) *Critical pulse regime (middle row)*: The spreading of energy over the BZ happens quickly and suppresses the peak at  $\mathbf{Q}$ . Till  $\sim 1000\tau_0$  there is no prominent feature in the BZ. Beyond this a peak at  $\mathbf{Q}$  reemerges and gains some weight. The intensity at the longest time,  $5000\tau_0$ , is far below what it was at  $t = 0$ . The associated Fourier transform looks very



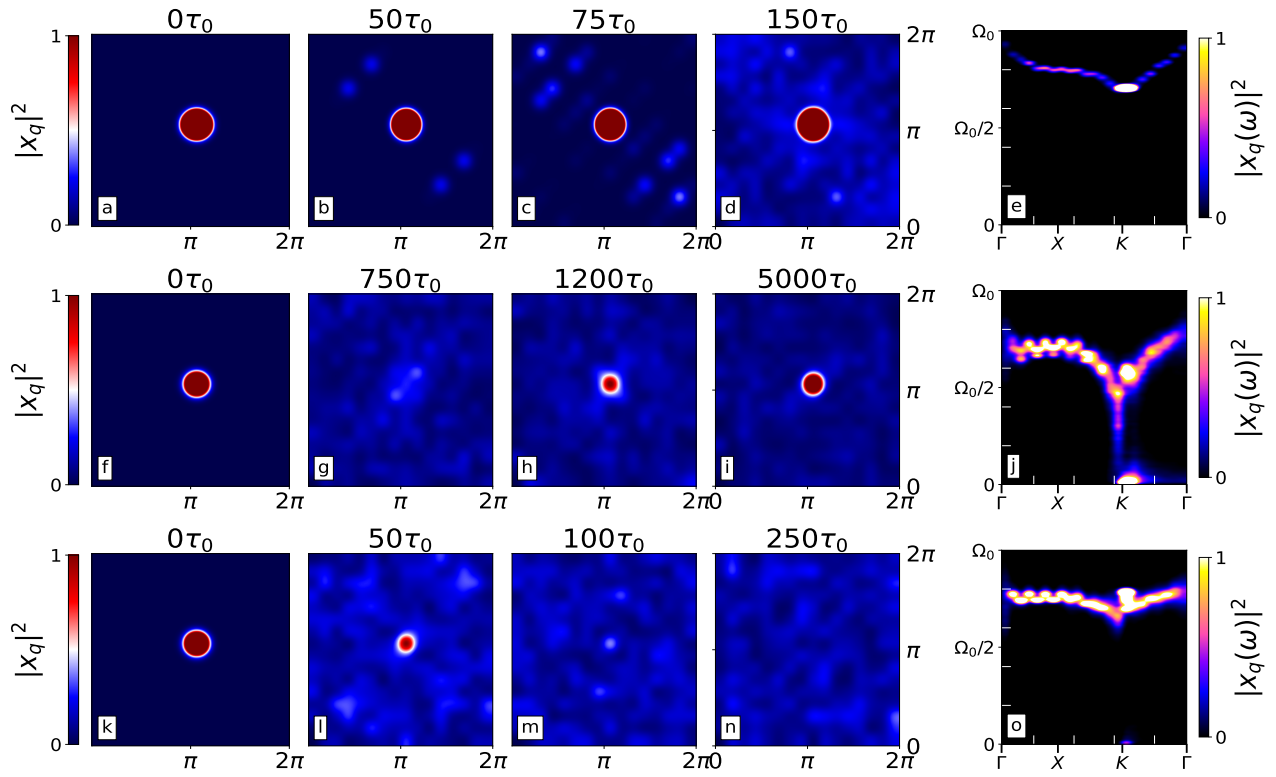


FIG. 11. The time dependence of  $|x_{\mathbf{q}}|^2$  over the entire Brillouin zone (BZ), and the associated frequency dependence, in the three pulse regimes. Top row: weak pulse ( $E_0 = 0.2$ ). (a-d) With increasing  $t$  first the intensity of  $\mathbf{q}$  modes along the diagonal increase and finally all  $\mathbf{q}$  modes become active. However the  $\mathbf{q} = \mathbf{Q}$  mode retains its dominant position. (e) shows the  $|x_{\mathbf{q}}(\omega)|^2$ , obtained via Fourier transform of  $x_{\mathbf{q}}(t)$  over the whole time range, on a selected path  $\Gamma(0, 0) - X(\pi, 0) - K(\pi, \pi) - \Gamma(0, 0)$  in  $\mathbf{q}$ -space. The response maps out the equilibrium phonon dispersion but with weight mostly centered at  $K$ -point. Middle row: critical regime ( $E_0 = 0.43$ ). (f-i) There is a quick transfer of energy to  $\mathbf{q}$  modes all over the Brillouin zone (BZ) and at  $t = 750\tau_0$  there is no peak at  $\mathbf{q} = \mathbf{Q}$ . By  $1200\tau_0$  there is a recovery and by  $5000\tau_0$  the intensity approaches the long time asymptote. (j) Frequency dependence reveals phonon band softening and broadening and a significant dip near  $K$ . Bottom row: strong pulse ( $E_0 = 0.7$ ). The timescales here are shorter than in the upper rows. The mode at  $\mathbf{Q}$  initially transfers energy along the diagonal of the BZ, which then cascades to the rest of the BZ. By  $t \sim 100\tau_0$  the energy has been distributed almost evenly over the BZ and there is no peak at  $\mathbf{q} = \mathbf{Q}$ . (o) The phonon-band starts flattening again and the mean frequency increases.

different from the linear response  $\Omega_{\mathbf{q}}$ , and is actually reminiscent of what one observes in the equilibrium problem near its thermal transition.

(iii) *Strong pulse regime (bottom row)*: The  $x_{\mathbf{Q}}$  amplitude diminishes monotonically with time and by  $\sim 100\tau_0$  there is no trace of the peak at  $\mathbf{Q}$ . The corresponding  $|x_{\mathbf{q}}(\omega)|^2$  shows an almost flat - momentum independent - oscillation, with uniform distribution of amplitude across  $\mathbf{q}$  similar to the equilibrium high temperature case. The  $\mathbf{q}$  space picture reveals how energy is distributed over the BZ as a function of time. It does not explain whether the destruction of CO, as in the critical and strong pulse regimes, occur due to imperfect ‘phase correlations’ between ordered domains, or due to the destruction of charge modulations itself. That requires examination of the spatial density  $n_i$  as a function of time.

### B. Spatial pattern and distribution functions

Fig.12 top row shows maps of  $n_i$  in the critical window. The main effect at intermediate time,  $\sim (10^2 - 10^3)\tau_0$ , is the

homogenisation of the charge density. We can call it ‘amplitude disordering’, in contrast to ‘phase disordering’ where modulations remain but interference between domains suppress order. For  $t \gtrsim 1500\tau_0$  the density modulations reappear, though much weaker than before, and spatially organise. At the longest time shown the  $n_i$  field has a well organised alternating pattern, though the modulations about  $n = 0.5$  are only  $1/3$  of the  $t = 0$  value, and there is some amplitude inhomogeneity. The disordering and revival seems to be an amplitude effect rather than a domain interference effect. Phase slippage, i.e. boundaries between the two complementary charge order states, CO and  $\overline{\text{CO}}$ , is not playing an important role in the delayed recovery. Rather, competition between the ‘metallic state’ (homogeneous density) and suppressed CO is seemingly playing the crucial role.

When comparing the pump driven decay and revival to the order parameter growth induced by thermal quench, some differences become apparent. In the thermal situation the competition between complementary ordered phases CO and  $\overline{\text{CO}}$  plays a more significant role. In equilibrium, the dynamics of the local distortions  $x_i(t)$  and density field  $n_i(t)$  are closely

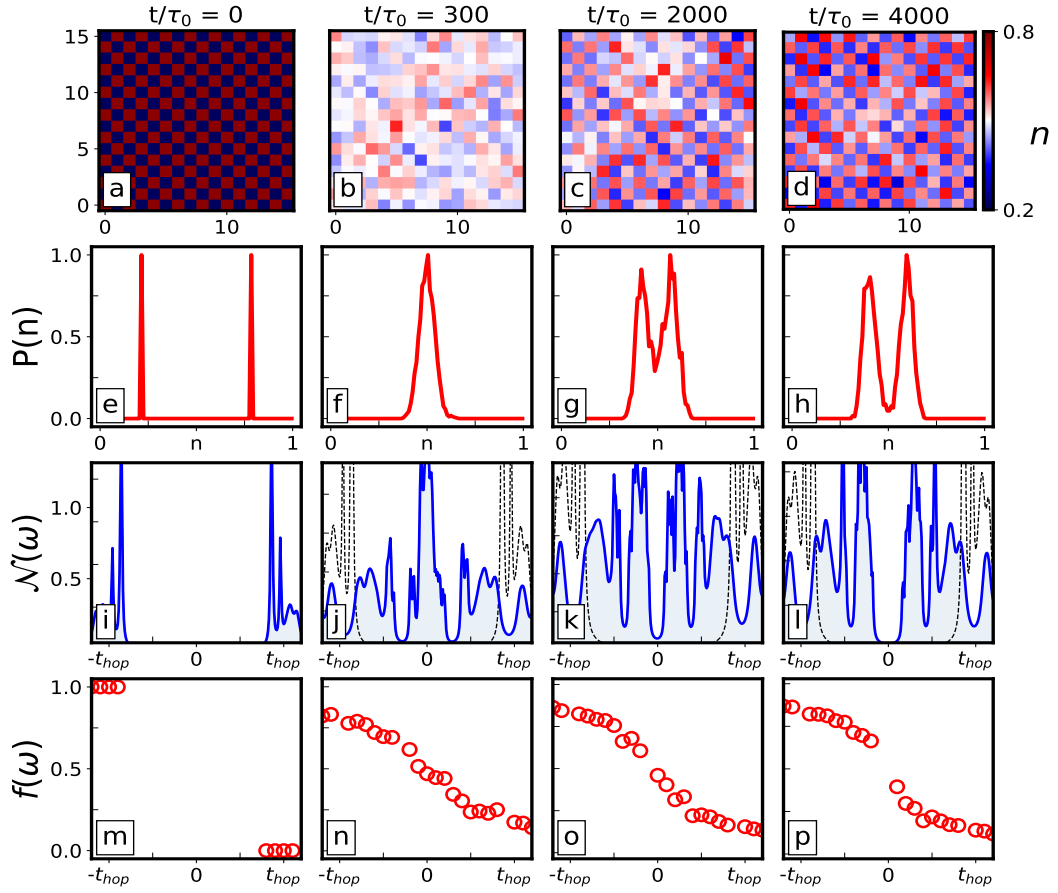


FIG. 12. Time dependence of spatial distribution and electronic properties in the critical pulse regime,  $E_0 = 0.45$ . First row: spatial variation of electron density  $n_i$ . At  $t = 0$  we have perfect checkerboard order  $n_i$  taking values  $\sim 0.2$  and  $0.8$  at alternate sites. Second row: the distribution of density  $P(n, t)$  corresponding to the spatial maps above. The  $P(n)$  is sharply bimodal. At  $t = 300\tau_0$  the  $n_i$  map show that charge modulations have essentially vanished, and  $P(n)$  shows an unimodal distribution peaked around  $n = 0.5$ . At  $t = 2000\tau_0$  we again see the re-emergence of charge modulations, a checkerboard structures, and a bimodal feature in  $P(n)$ . The last column show the ‘revived’ charge density, now varying roughly between  $0.4$  and  $0.6$ . This is roughly  $1/3$  the charge modulation in the  $t = 0$  state. The  $P(n)$  has a clearer bimodal feature now. Third row: density of states  $\mathcal{N}(\omega)$  based on the instantaneous eigenvalues in the  $x_i(t)$  background. At  $t = 0$  there is a gap  $\sim 1.6t_{hop}$ . The gap closes around  $\sim 300\tau_0$  and starts to reopen around  $\sim 2000\tau_0$ . It reaches a saturation value  $\sim 0.5t_{hop}$  around  $\sim 4000\tau_0$ . Fourth row: the occupation function  $f(\omega, t)$ . The pre-pump distribution is the zero-temperature Fermi function. The pump depletes low energy states and creates population at significantly high energies. After the gap reopens a large upper-band population still retains.

correlated. At very low temperatures, the system assumes a CO state among the two symmetry-broken states (with  $Z_2$ -like symmetry). However, at temperatures higher than the CO melting temperature  $T_{CO}$ , though local distortions are present, the presence of domains reduces long-range order, leading towards zero structure factor. Even if the system is thermally quenched, this domain growth alone is responsible for the delay in order parameter recovery.

In the photo-induction case, a laser pulse quickly melts this equilibrium distortion in  $n_{\mathbf{Q}}(t)$ , inducing an excess energy in  $x_{\mathbf{Q}}(t)$ , resulting in ringing in  $x_{\mathbf{Q}}(t)$ . However, the dynamics of  $x_{\mathbf{Q}}(t)$  are not solely determined by the coupling to other phonon modes; electrons also play a crucial role, resulting in effective dissipation. Estimation of this dissipation is discussed in Sec. VI.

Due to this, the local distortions themselves reduce, and a combination of amplitude as well as domain growth plays an

important role in the recovery of the order parameter. This is evident when we look at the destruction of the bimodality in the distribution function  $P(n)$  discussed below.

The second row shows the distribution of densities,  $P(n)$ , at different times. At  $t = 0$ ,  $P(n)$  shows a bimodal structure with  $\pm 0.3$  modulation around  $n = 0.5$ . The post-pump state at  $300\tau_0$  shows a single peak centred at the mean density  $n = 0.5$ . Around  $t = 1500\tau_0$  this starts to broaden, showing a hint of bimodality, and spatial configuration shows patches of charge order (CO). At  $t = 2000\tau_0$  we see a clear bimodal structure which sharpens by  $4000\tau_0$ .

The third row shows the instantaneous DOS at different times obtained by binning the eigenvalues  $\epsilon_n(t)$  of the electronic Hamiltonian in the background  $x_i(t)$ . The pre-pump state has a gap  $\sim 1.5t$ . At  $t \sim 300\tau_0$  the gap has vanished and the DOS shows a prominent peak at  $\omega = 0$ . Beyond this, with increasing  $t$ , as the lattice distortions increase and organise in

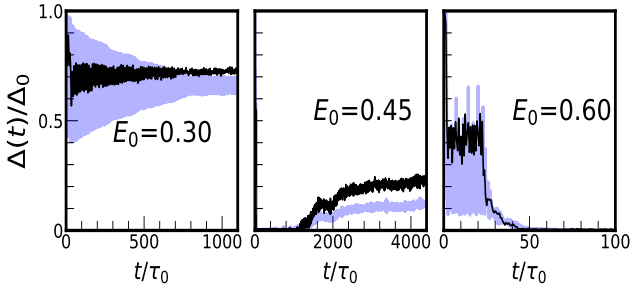


FIG. 13. Behaviour of the gap in the electronic DOS (black) computed from the instantaneous spectrum at different  $E_0$ . In weak pulse regime,  $E_0 = 0.3$ ,  $\Delta(t)$  oscillates then relaxes to 70% of  $\Delta_0$ . In critical regime,  $E_0 \sim 0.45$ ,  $\Delta(t)$  shows suppression and revival. In the strong pulse regime,  $E_0 = 0.6$ ,  $\Delta(t)$  goes to zero by  $\sim 50\tau_0$ .  $\Delta(t)$  is closely correlated with  $|x_{\mathbf{Q}}(t)|^2$  (blue). Both  $\Delta(t)$  and  $|x_{\mathbf{Q}}(t)|^2$  were normalized by their initial equilibrium value.

the  $(\pi, \pi)$  pattern again, spectral weight is lost at low energy. At  $t = 2000\tau_0$  a small gap shows up in the spectrum which grows to about  $\sim 1/3$  of the  $t = 0$  value at the longest time,  $4000\tau_0$ .

In contrast to the equilibrium state at zero temperature, where electronic occupancy is dictated by a sharp Fermi distribution, in the post pump situation the occupancy of the instantaneous eigenstates is time dependent and non zero for  $\omega > 0$  states as well. The bottom row illustrates the occupation of these levels derived from  $\rho_{nn}(t)$  by projecting  $\rho_{ij}$  onto the instantaneous eigenvectors. At  $t = 0$ , i.e before the pulse, it is the usual Fermi function  $\theta(-\omega)$ . The pump induces transitions to the upper band. By  $t \gtrsim 300\tau_0$  the post-pump distribution assumes a smooth form. Subsequently, as the gap begins to open around  $2000\tau_0$ , a significant population of excited electrons  $n_{exc}$  remains in the upper band. In this particular case,  $n_{exc}$  amounts to approximately 25%.

Fig.13 quantifies the time dependence of the gap  $\Delta(t)$  inferred from the instantaneous spectrum. In the weak pulse regime the gap  $\Delta(t)$  (normalized by  $\Delta_0$ ) shows oscillatory behaviour, followed by a relaxation to a slightly suppressed value. For example at  $E_0 \sim 0.3$  it stabilises to  $\sim 70\%$  of its original value. In the critical regime, the instantaneous gap shows an oscillatory behaviour but averaged over a  $10\tau_0$  time scale (black line) it shows suppression and revival dynamics. In strong pulse regime, the gap goes to zero within  $\sim 100\tau_0$ . It can be noticed that this normalized gap is closely correlated with the normalized  $|x_{\mathbf{Q}}(t)|^2$  as shown in the figure with faint blue line.

## VI. RESULTS FROM A SIMPLE CLASSICAL MODEL

Full mean field dynamics is expensive since it involves a  $\mathcal{O}(N^2)$  process for every microscopic step  $\delta t$ . The dynamics needs to be tracked to a time  $\tau_{max}$ , that is needed to reach the asymptotic state, and  $\tau_{max}$  grows with system size.

The electron-phonon problem has a hierarchy of timescales,  $\delta t \ll t_{hop}^{-1} \ll \tau_0 \ll \tau_{max}$ . Typically  $\delta t \sim 10^{-3}\tau_0$  and

$\tau_{max} \sim 10^4\tau_0$ . That indicates that the  $\mathcal{O}(N^3)$  diagonalisation has to be done  $\sim 10^7$  times. limiting us to sizes  $\sim 20 \times 20$ . While the qualitative physics of suppression, revival, and loss of order is accessible on this spatial and time scale a simpler model, with much greater spatio-temporal reach, can be motivated from the lessons in the last section.

These are: (i) The pump creates an ‘upper band’ population that decays to non zero value over a short timescale. This excited population  $n_{exc}$  persists over a very long time and can be approximated by a Fermi distribution with some temperature  $T_{el}$ . This affects the magnitude and ordering of the lattice distortions. (ii) The effective temperature of the phonon system and the electron system are not the same on timescales that we probe.  $T_{el}$  is dictated by  $n_{exc}$ , we discuss  $T_{ph}$  later. (iii) There is the usual growth and interference of CO domains as with any ordering phenomena. This needs to be handled in a real space setting.

This requires a model that captures large distortion physics non perturbatively, incorporates intersite coupling that promotes a checkerboard pattern, and a mechanism to sense the population of excited electrons.

### A. Constructing the model

The simplest model for large distortion induced electron trapping is one electron on two sites (one electron on one site is trivial since the hopping term is absent). For this the electronic part of the model is:

$$H_2^{el} = -t_{hop}(c_1^\dagger c_2 + c_2^\dagger c_1) - g(n_1 x_1 + n_2 x_2)$$

Treating the  $x$  as classical, the two eigenvalues of this are elementary:

$$\lambda_{\pm} = -\frac{gx_{\pm}}{2} \pm \sqrt{\frac{g^2 x_{\pm}^2}{4} + t_{hop}^2}$$

where  $x_{\pm} = x_1 \pm x_2$ . If the electrons sense an effective temperature  $T_{el}$ , that creates the upper level population, then the free energy associated with the electronic part is

$$F_{el}(x_1, x_2) = -T_{el} \ln(e^{-\beta_{el}\lambda_-} + e^{-\beta_{el}\lambda_+})$$

Adding the stiffness terms, the effective ‘potential’ dictating the dynamics of the  $x_i$  is

$$V(x_1, x_2) = \frac{K}{2}(x_1^2 + x_2^2) + F_{el}(x_1, x_2)$$

A couple of comments before we generalise  $V$  to the lattice, i.e, construct an approximate  $V(x_1, \dots, x_N)$ .

(i) The potential is symmetric under the interchange of  $x_1$  and  $x_2$ . (ii) For  $T_{el} \rightarrow 0$  we have  $F_{el} \rightarrow \lambda_-$  and minimising with respect to  $x_+$  and  $x_-$  leads to

$$\bar{x}_+ = \frac{g}{K}, \quad \bar{x}_- = \pm \frac{1}{g} \sqrt{\left(\frac{g^2}{K}\right)^2 - t^2}$$

(iii) At large  $g$  the lowest eigenvalue can arise from two  $x$  configurations:  $(x_1 = g/K, x_2 = 0)$  and its complement.

The corresponding charge density would be (1, 0) or (0, 1). (iv) We will see later that as  $T_{el}$  increases the tendency to have a modulation  $x_-$  reduces.

Putting these together we propose a phonon model of the form

$$H_{ph}^{eff} = \sum_i \frac{p_i^2}{2M} + \frac{K}{2} \sum_i x_i^2 + \frac{1}{z} \sum_{\langle ij \rangle} V(x_i, x_j)$$

$$V(x_i, x_j) = -T_{el} \ln(e^{-\beta_{el}(\lambda_-(x_i, x_j) - \mu)} + e^{-\beta_{el}(\lambda_+(x_i, x_j) - \mu)})$$

Here  $z$  is the number of nearest neighbours. In 2D, it is 4.  $\mu$  is the chemical potential set to half filling condition in equilibrium. The parameters involved in  $H_{ph}^{eff}$  are all defined already in the Holstein model, except for  $T_{el}$  - which we extract by fitting the excited population in the full MFD to a thermal distribution. That is, the MFD based  $n_{exc}(t, E_0)$  is mapped on to a  $n_{exc}(t, T_{el})$ . Thankfully the time dependence of  $T_{el}$  is simple - it settles to its long time value quickly and the lattice dynamics plays out in the background of this ‘final’ electron temperature  $T_{el}^f$ .

The effective potential for two sites can be written as  $V(x_+, x_-) = V_1(x_-) + V_2(x_+)$  and at half filling, this assumes the form

$$\begin{aligned} V_1(x_-) &= \frac{1}{4} K x_-^2 - T_{el} \ln[e^{-\beta_{el} \bar{\lambda}} + e^{+\beta_{el} \bar{\lambda}}] \\ V_2(x_+) &= \frac{1}{4} K x_+^2 - \frac{1}{2} g x_+ \\ \bar{\lambda}(x_-) &= \sqrt{\frac{1}{4} g^2 x_-^2 + t_{hop}^2} \end{aligned}$$

In Fig.14 we plot this 2 site effective potential as a function of  $x_1$  and  $x_2$  and we get two wells around (0,  $g/K$ ) and ( $g/K$ , 0) at  $T_{el} = 0$  (left). When we plot the  $V(x_-)$  with  $T_{el}$  with  $x_+ = g/K$  we see a transition from double well to a single well around  $T_{el}/E_p \sim 0.5$ . Near this critical excitation  $T_{el}^c$  the  $x_- \rightarrow 0$ ,  $x_+ \rightarrow 2 \times x_{av}$ , where  $x_{av}$  is the mean  $x$  over the lattice ( $g/2K$ ). In this limit the function can be expanded in powers of  $\xi_i = x_i - x_{av}$  and have the form

$$V(\xi) = \sum_i (A \xi_i^2 + B \xi_i^4) + C \sum_{ij} \xi_i \xi_j$$

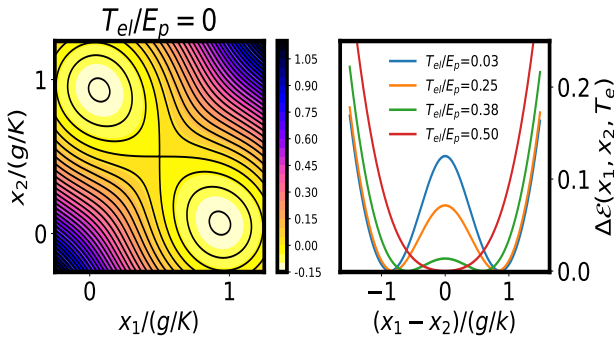


FIG. 14. (a) Effective potential  $V(x_1, x_2)$  at  $T_{el} = 0$ , and (b) the nature of  $V(x_1 - x_2)$  with increasing  $T_{el}$ .

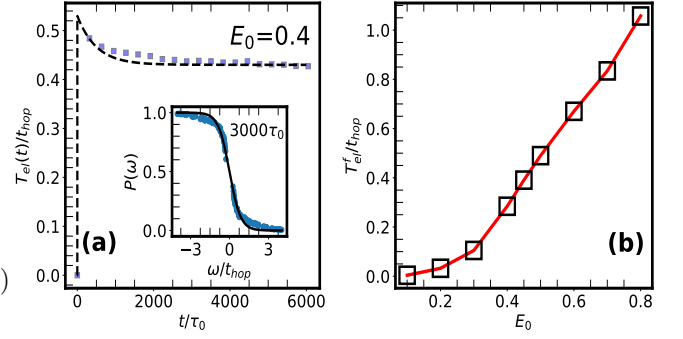


FIG. 15. Extracting an ‘electronic temperature’: (a) the population function  $P(\omega)$  obtained from MFD is fitted to a Fermi function with temperature  $T_{el}(t)$ .  $T_{el}$  settles down to a value  $T_{el}^f$  over a timescale  $\tau_{el}$  - the fit is shown (see comments in text). The inset shows the Fermi function fit. (b) The long time value of  $T_{el}$  for varying  $E_0$ . This is the crucial factor in deciding the existence of long range order.

and higher order intersite terms. Here,

$$\begin{aligned} A(T_{el}) &= \frac{1}{2} (K - \frac{g^2}{4t_{hop}} \tanh[\frac{t_{hop}}{T_{el}}]) \\ B(T_{el}) &= \frac{g^4}{32t_{hop}^3} (\tanh[\frac{t_{hop}}{T_{el}}] - \frac{t_{hop}}{T_{el}} \text{sech}^2[\frac{t_{hop}}{T_{el}}]) \\ C(T_{el}) &= \frac{g^2}{8t_{hop}} \tanh[\frac{t_{hop}}{T_{el}}] \end{aligned}$$

## B. Scheme for dynamics

With the excited electron population specified by  $T_{el}$  the effective ‘force’ driving  $x_i$  is  $-Kx_i - (\partial V/\partial x_i)$ . If the  $x_i$  sense a thermal environment with temperature  $T_{ph}$  then the equation dictating  $x_i$  dynamics would be:

$$M \frac{d^2 x_i}{dt^2} = -\frac{\partial H_{ph}^{eff}}{\partial x_i} - \gamma \frac{dx_i}{dt} + \eta_i$$

where  $\gamma$  is a dissipation parameter and  $\eta$  is a random white noise satisfying:

$$\langle \eta_i(t) \rangle = 0, \quad \langle \eta_i(t) \eta_j(t') \rangle = 2\gamma T_{ph} \delta_{ij} \delta(t - t')$$

Both  $T_{ph}$  and  $\gamma$  enter in our calculations as phenomenological constants. However, we can make an estimate of these phenomenological constants from the MFD. The equation for oscillator in MFD is,  $M \frac{d^2 x_i}{dt^2} = -Kx_i + g\rho_{ii}$ . This on-site density  $\rho_{ii}$  can be written as the instantaneous term (calculated from the phonon background with electronic population) and its fluctuation as  $\rho_{ii} = n_i^{inst} + \delta n_i(t)$ . We assume this fluctuation to be of form  $g\delta n_i(t) = -\gamma \frac{dx_i}{dt} + \eta_i(t)$ . At large frequency  $|\delta n_i(\omega)|^2$  only contributes to  $|\eta_i(\omega)|^2$  which, is a constant  $\frac{2}{g^2} \gamma T_{ph}$ . From this we get an estimate for  $\gamma T_{ph} \sim 10^{-5} t_{hop}$  at  $E_0 \sim 0.4$ . In Fig.16, we get an estimate of  $T_{ph}/t_{hop}$  which is between  $10^{-3}$  to  $10^{-4}$ . So, our estimate for  $\gamma$  is of order  $10^{-2}$  to  $10^{-1}$ .

### C. Electron population and Langevin parameters

From the MFD we can track the excited population  $n_{exc}(t, E_0)$  and map it to a  $T_{el}(t, E_0)$ . Fig.15(a) shows such a time dependent profile for  $T_{el}$  and the inset shows a long time distribution function that is fitted by a Fermi function. The time dependence of  $T_{el}$  can be fitted to:

$$T_{el}(t, E_0) = T_{el}^i e^{-t/\tau_{el}} + T_{el}^f(E_0)(1 - e^{-t/\tau_{el}})$$

our MFD suggests  $\tau_{el} \approx 10\tau_0$ , while  $T_{el}^f$  depends on  $E_0$  in the manner shown in Fig.15(b). We now set the rest of the parameters,  $t_{hop} = 1$ ,  $g = 2$ ,  $M = 25$ ,  $K = 1$ ,  $\tau_0 = 2\pi/\sqrt{K/M}$ ,  $E_p = g^2/2K$ .  $\gamma = 0.05$ ,  $T_{ph}/t_{hop} = 10^{-3}$ .  $T_{el}^f$  is varied keeping  $T_{el}^i/T_{el}^f = 1.1$ . We study  $L \times L$  geometry with  $L = 30, 40, 60, 80, 100$ .

### D. Results on order parameter loss-recovery dynamics

Our investigation of this classical model reveals three distinct regimes dependent on  $T_{el}^f$ , akin to the findings in MFD. Slight variations in  $T_{el}^f$  (below  $T_{el}^f \sim 0.3E_p$ ) induce oscillations in  $x_{\mathbf{Q}}(t)$ , similar to ringing. These oscillations dampen over time due to the phenomenological damping  $\gamma$ , with a time scale proportional to  $\tau_w \sim 1/\gamma$ . However, this time scale remains constant by design in this simplified model and cannot capture the variation of dissipation time with pump excitation. Similarly, for  $T_{el}^f > 0.455 E_p$ , no recovery occurs, and the dissipation time scale is determined solely by  $\gamma$ . We focus in Fig.17 on the critical dynamics window. In 17.(a), we observe the loss and recovery dynamics in  $|x_{\mathbf{Q}}(t)|$ . As  $T_{el}^f \rightarrow 0.45E_p$ , a transition becomes evident. We fit the recovery part of  $|x_{\mathbf{Q}}(t)|$  with  $|x_{\mathbf{Q}}(t)| \sim X_0 e^{-(\tau_r/t)^\beta}$  where  $X_0 = |x_{\mathbf{Q}}(\infty)|$  and  $\beta$  ranges from 4 – 6. In 17 (b), we depict the dependence of  $|x_{\mathbf{Q}}(\infty)|$  and  $\tau_r$  on  $T_{el}^f$ . The recovered

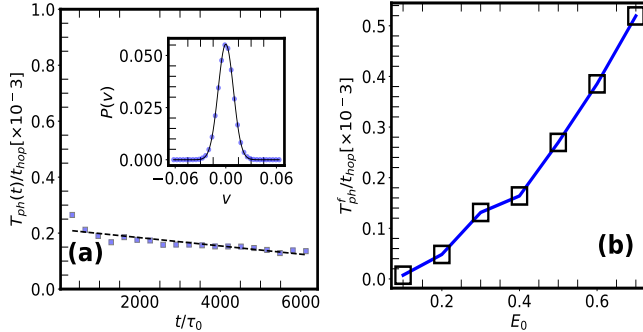


FIG. 16. Extracting an ‘phonon temperature’: (a) the distribution function  $P(v)$  constructed from velocity  $\langle p_i \rangle / M$  which was obtained from MFD is fitted to a Maxwell-Boltzmann function with temperature  $T_{ph}(t)$ .  $T_{ph}$  is almost constant around a value (For  $E_0 = 0.4$ , it is  $2 \times 10^{-4}$ ) which much lower than the  $T_{el}^f$ . The inset shows the distribution function fit. (b) The long time value of  $T_{ph}$  for varying  $E_0$ .

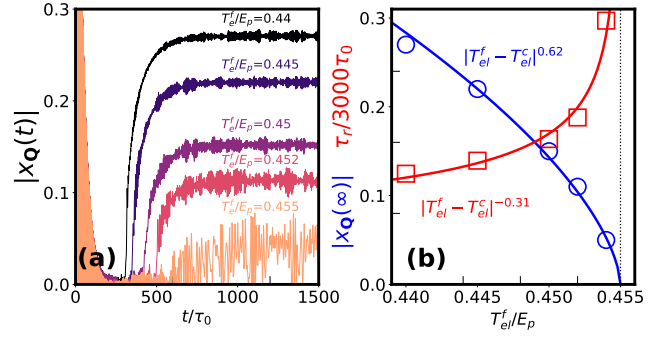


FIG. 17. In (a) the loss and revival dynamics of  $|x_{\mathbf{Q}}(t)|$  with varying  $T_{el}^f$  is shown. (b) As  $T_{el}^f/E_p \rightarrow 0.455$ ,  $|x_{\mathbf{Q}}(t)| \rightarrow 0$  and recovery timescale  $\tau_r$  diverges. These results are on  $40 \times 40$  lattice size. We show a fit  $|x_{\mathbf{Q}}| \sim |T_{el}^f - T_{el}^c|^\alpha$  near the critical regime and we find  $\alpha \sim 0.62$ . The  $\tau_r$  shows divergence as  $\tau_r \sim |T_{el}^f - T_{el}^c|^{-\nu}$  with  $\nu \sim 0.31$ .

$|x_{\mathbf{Q}}|$  exhibits scaling  $\sim |T_{el}^f - T_{el}^c|^\alpha$ , with  $\alpha = 0.62$ . The recovery time is fitted with  $\tau_r \sim |T_{el}^f - T_{el}^c|^{-\nu}$  with  $\nu = 0.31$ .

Fig.18 top panel illustrates the real space dynamics of domain formation and growth in a system sized  $60 \times 60$  with  $T_{el}^f = 0.45 E_p$ . In equilibrium, lattice distortions exhibit a modulation of approximately  $\sim g/2K$  around the mean distortion, which is also  $\sim g/2K$ . By subtracting the average distortion  $g/2K$  at each site and multiplying by a periodic modulation  $e^{i\mathbf{Q} \cdot \mathbf{r}_i}$ , we homogenize the periodic structure to a positive ( $C$ -state) or negative ( $C'$ -state) uniform field in the perfectly charge ordered (CO) background. In the absence of a background CO structure, the amplitude is zero - we term it the  $M$ -state.

Following the ‘pump,’ the initial  $C$ -state diminishes, and around  $t \sim 150\tau_0$ , equal amounts of  $C$ ,  $C'$ , and  $M$ -type exist in a short range correlated manner. By  $t \sim 350\tau_0$ , the  $C$  and  $C'$  states begin to dominate, and a domain competition ensues with  $C$  eventually prevailing around  $t \sim 450\tau_0$ . The middle panel depicts the structure factor  $|x_{\mathbf{q}}|^2$ , reflecting the loss and recovery of weight at  $\mathbf{q} = \mathbf{Q}$ . The bottom row shows the time dependence of the  $P(x)$  distribution. The sharp bimodal feature at  $t = 0$  homogenizes by  $150\tau_0$  and persists until  $300\tau_0$ , before a broadened distribution reemerges around  $350\tau_0$ . By  $500\tau_0$ , a ‘long time’ distribution emerges with a much smaller modulation in  $x$  compared to  $t = 0$ .

### E. Identification of three regimes from the classical model

As a result of increasing  $T_{el}^f$  the  $x_{\mathbf{Q}}(t)$  in 2D shows similar dynamical regimes- WOS, SSR, MS as shown in Fig. 19. Similar analog of these regimes can be seen in  $x_-(t)$  for 2 site. We examine the energetics of the 2-site model first, in response to an increase in  $T_{el}$  and then move to the lattice model. In the 2-site setup, the key variable is  $x_- = x_1 - x_2$ , a crude mimic of  $x_{\mathbf{Q}}$  on the lattice. We denote  $x_-$  by  $y$  in what follows. The effective potential  $V_{eff}(y, T_{el})$ , depicted in Fig.14, reveals a double-well structure with pre-pulse minima

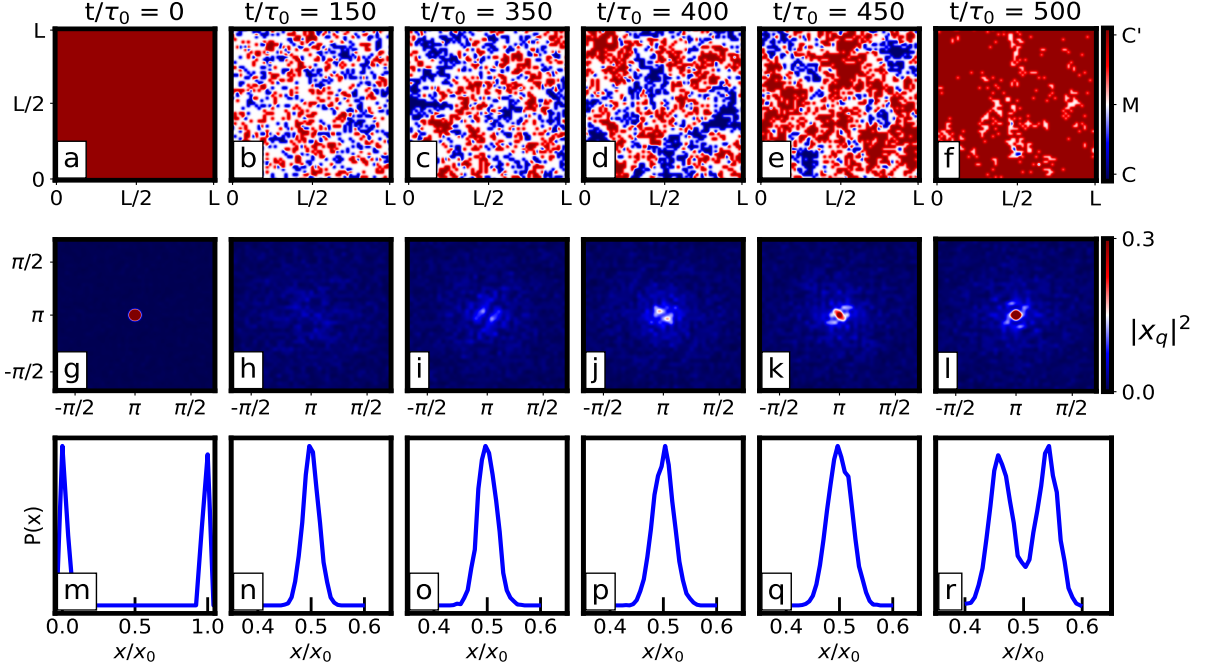


FIG. 18. Suppression and revival dynamics in the 2D classical model with  $T_{el}^f = 0.45E_p$  on a  $60 \times 60$  lattice. The top row shows charge order domains (see text). Red represents the  $C$  type checkerboard pattern, blue denotes the phase shifted state  $C'$ , while white indicates no modulations - referred to as the  $M$  state. At  $t = 0$ , a perfect  $C$ -state exists, disrupted by the pump over time. At approximately  $150\tau_0$ , equal amounts of red, white, and blue domains emerge. Around  $350\tau_0$ , blue and red domains start to cluster, reducing the  $M$ -state, leading to a CO state  $C$  by  $500\tau_0$ . The middle panel shows  $|x_q|^2$  with the suppression and recovery of the  $(\pi, \pi)$  peak with time. The bottom row displays time dependence of the  $P(x)$  distribution. The sharp bimodal feature at  $t = 0$  homogenizes by  $150\tau_0$ . This persists to  $300\tau_0$ , before a broadened distribution reemerges around  $350\tau_0$ . At  $500\tau_0$ , the ‘long time’ distribution appears with a much smaller modulation in  $x$  compared to  $t = 0$ .

at  $\pm y_{min}(T_{el} = 0)$ . An abrupt change in  $T_{el}$  alters the minima locations to a suppressed value  $\pm y_{min}(T_{el})$ , accompanied by a reduction in the ‘barrier height’  $\Delta_b(T_{el})$  between the minima and the maximum. Alteration of the potential makes the original minimum a ‘high energy’ location now, with an excess energy

$$\mathcal{E}(T_{el}^f) = V(y_{min}(0), T_{el}^f) - V(y_{min}(T_{el}^f), 0) - \Delta\mathcal{E}(T_{el})$$

Where,  $\Delta\mathcal{E}(T_{el}) = V(0, T_{el}^f) - V(0, 0)$ . The two site problem cannot settle down into its new minimum unless this excess energy is dissipated. We categorize the possibilities as follows: (i) Suppressed Oscillations ( $0 \leq T_{el}^f \leq T_{el}^w$ ): As  $T_{el}^f$  increases, the excess energy  $\mathcal{E}(T_{el}^f)$  rises while  $\Delta_b(T_{el}^f)$  begins to decrease. At  $T_{el}^f = T_{el}^w$ , these values intersect ( $\mathcal{E}(T_{el}^f) = \Delta_p(T_{el}^f)$ ). For  $T_{el}^f < T_{el}^w$ , oscillations in  $|x_-(t)|$  are confined to a single well within the system. Dissipation causes  $\mathcal{E}(T_{el}^f)$  to decay as  $\sim \mathcal{E}(0)e^{-\gamma t}$ , and  $|x_-(t)|$  stabilizes to the steady-state value  $|x_-(T_{el}^f)|$  over a time scale  $\tau_w \sim \frac{1}{\gamma}$ .

(ii) Monotonic Suppression ( $T_{el}^f > T_{el}^c$ ): If  $T_{el}^f$  surpasses the critical value such that  $\Delta_b(T_{el}^f) = 0$ , no double-well structure exists in  $V(x_1 - x_2, T_{el}^f)$ . The  $|x_1(t) - x_2(t)|$  decays to a homogeneous state with a similar time scale  $\sim \frac{1}{\gamma}$ .

(iii) Loss and Recovery ( $T_{el}^w \leq T_{el}^f \leq T_{el}^c$ ): In this regime, despite the presence of a double well in  $V(x_1 - x_2, T_{el}^f)$ , the

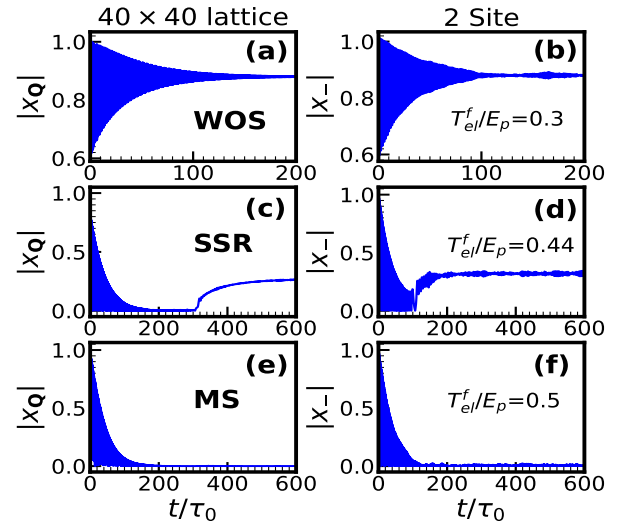


FIG. 19. In the first panel, we observe weak oscillatory suppression (WOS) with  $T_{el}^f/E_p = 0.3$  in  $x_Q$  on a  $40 \times 40$  lattice (a). In (b), we observe similar dynamics in  $x_-$ . Both are normalized to their equilibrium value. Panels (c) and (d) show strong suppression and recovery (SSR) dynamics at  $T_{el}^f/E_p = 0.44$ . While their revival values are the same, their dynamics differ in detail. At  $T_{el}^f/E_p = 0.5$ , we observe monotonic suppression (MS) in both the 2D and 2-site cases (e-f).

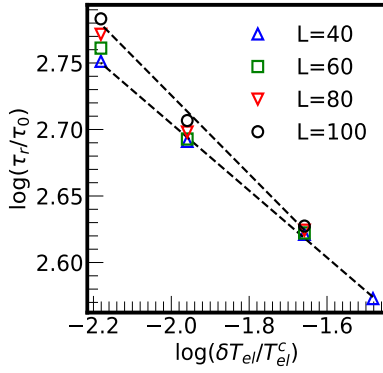


FIG. 20. Log-log plot of the recovery time  $\tau_r$  vs  $\delta T_{el} = |T_{el}^f - T_{el}^c|$  for different system sizes. The difference in recovery time increases with system size faster for small values of  $\delta T_{el}$ . We plot this for  $L=40, 60, 80, 100$ . Dotted lines correspond to linear fittings to  $L=40$  and  $L=100$  system sizes.

excess energy is significant enough to facilitate  $x_1(t) - x_2(t)$  transitioning between wells. This  $x_1(t) - x_2(t)$  can condense into one of the wells of  $V(x_1 - x_2, T_{el}^f)$  when  $\mathcal{E}(t = \tau_r, T_{el}^f) = \Delta_b(T_{el}^f)$ . Hence,  $\tau_r = \frac{1}{\gamma} \ln(\mathcal{E}(T_{el}^f)/\Delta_b(T_{el}^f)) \sim F(T_{el}^f) - \frac{1}{\gamma} \ln(\Delta_b(T_{el}^f))$ . Here,  $F(T_{el}^f)$  is non-critical. This divergence of the timescale in this case is purely local. Nonetheless, this analysis showcases how three regimes can arise due to changes in  $T_{el}$ , even in a 2-site problem as shown in Fig 19.

In 2D, these regimes are also present and the corresponding  $T_{el}$  values also match at regime boundaries. For ‘WOS’ and ‘MS’ we see similar dynamics in  $x_Q$  as shown in Fig.19. In the 2D classical model, however, the relaxation toward the steady state in ‘SSR’ regime encompasses both amplitude growth and spatial organization, which are intricately intertwined, evident in the broad width of the distribution  $P(x)$ . To analyze this, in Fig 20, we plot the recovery time  $\tau_r$  against  $\delta T_{el} = |T_{el}^f - T_{el}^c|$  for various system sizes  $L = 40, 60, 80, 100$ . Notably, the disparity in recovery time escalates more rapidly with increasing system size, particularly pronounced for smaller values of  $\delta T_{el}$  but the base value on top of which it grows is already very large indication a weak system size dependence.

## VII. DISCUSSION

### A. Size effects in MFD: locating the critical point

The MFD computation time scales as  $N^2 N_\tau$ , where  $N$  is the number of lattice sites and  $N_\tau$  is the number of integration timesteps in the interval  $[0 - \tau_{max}]$ . Within resource limits, we could access  $N \sim 400$  and  $N_\tau \sim 10^6$  (involving about  $10^4 - 10^5$  phonon oscillations). While this was adequate in the weak and strong pulse regimes, accessing the critical regime, where the recovery time  $\tau_{cr}$  diverges as  $E_0 \rightarrow E_0^c$ , was difficult. We had to extract the  $t \rightarrow \infty$  value of  $x_Q$  by fitting. Fig. 21 shows the result of  $x_Q(t \rightarrow \infty)$  as a function of  $E_0$  for different  $L$ .

We fit  $|x_Q|^2$  to  $|E_0 - E_0^c|^\alpha$ , which suggests  $E_0^c \sim 0.48$  with  $\alpha = 0.7$ . Similarly,  $\tau_r$  demonstrates a good fit with  $|E_0 - E_0^c|^{-\nu}$ , where  $\nu \sim 0.45$ . However, due to the size limitations of our simulations, we must acknowledge that these exponents are not definitive. We have done our best to fit the data to our current knowledge, but larger system sizes would be required to precisely determine the critical exponents.

### B. Thermalisation

Mean field theory of a photo-pumped system often cannot capture the eventual thermalisation, the effective electron and phonon temperatures remain different. To that extent one could ask what is the relevance of the long time state that emerges in our calculations. There are two aspects we briefly comment on (i) an estimate of the thermalisation time based on work that has been done on other gapped systems, and (ii) the comparison of the state that we obtain at a pump intensity  $E_0$ , and associated excess energy  $\Delta\mathcal{E}$ , with the equilibrium state that would have resulted if the system had excess thermal energy  $\Delta\mathcal{E}$ .

Regarding thermalisation time specific calculations have been done on Mott insulators. The conclusion there is that a pump pulse excites electrons across the gap  $\Delta$ , creating double occupancy, and these electrons deexcite by multimagnon emission, each magnon having an energy  $\sim J = 4t^2/U$ , where  $U$  is the Hubbard repulsion. An early estimate of the decay time was provided by Strohmaier et al [54] who suggest a result of the form  $\tau_D \sim \frac{\hbar}{J} e^{(\alpha \frac{U}{zJ})}$ , where  $z$  is the coordination number of the lattice. The coefficient  $\alpha \sim \mathcal{O}(1)$ . The essence of this result is that the time for emitting multiple ‘bosons’, each of energy  $\sim zJ$ , to deexcite an electron at an energy  $U \gg zJ$  is exponentially large. The emission processes have to act in sequence. This was established through an exact diagonalisation calculation by Lenarcic and Prelovsek [55]. We are not aware of an equivalent calculation for the Hol-

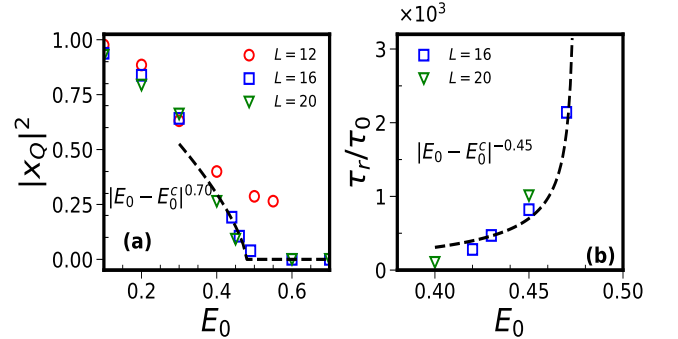


FIG. 21. We show (a)  $|x_Q|^2$  and (b) recovery time  $\tau_r$  (b) obtained from MFD for various system sizes. Fitting  $|x_Q|^2$  to  $|E_0 - E_0^c|^\alpha$  suggests a critical value  $E_0^c \sim 0.48$  with  $\alpha = 0.7$ . For a given  $\tau_{max}$ , capturing  $\tau_r$  for larger systems ( $L = 20$ ) proves challenging, while for  $L = 12$ , the system exhibits unclear loss-recovery dynamics. Notably, for  $L = 16$ ,  $\tau_r$  demonstrates a good fit with  $|E_0 - E_0^c|^{-\nu}$ , where  $\nu \sim 0.45$ .

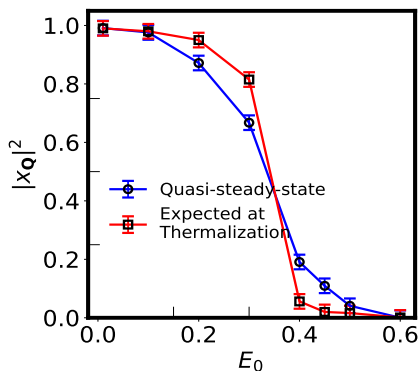


FIG. 22. Associated with the laser pulse amplitude  $E_0$  we calculate the excess energy  $\Delta\mathcal{E}$  and compare the structure factor  $|x_{\mathbf{Q}}|^2$  at steady state (blue) with the system with same  $\Delta\mathcal{E}$  at thermal equilibrium (red). This suggests if the system was able to redistribute its excess energy and reach an internal thermalisation, the structure factor would be similar though the nature of the suppression would change from amplitude driven to fluctuation driven.

stein model but the physical process invoked in the Mott insulator suggests that electrons excited across the charge ordering gap  $\Delta_{CO}$  would deexcite by emitting phonons with energy  $\sim \hbar\Omega_0$ . In model problem the gap is  $\Delta_{CO} \sim 1.5t_{hop}$  and the phonon frequency is  $\sim \hbar\Omega_0 = 0.2t_{hop}$ . Even with intersite coupling the phonons have a narrow band of energies around  $\hbar\Omega_0$ . As a result, following, Strohmaier et al, we expect  $\tau_D \sim \tau_0 \exp(\frac{\Delta_{CO}}{\hbar\Omega_0})$ . At our parameter point this is  $\sim 1800\tau_0$ . So, in a fuller calculation we expect that the intermediate time dynamics that we see, on the scale of few hundred  $\tau_0$ , would remain, but at longer times the upper band population will relax leading to a common temperature for phonons and electrons. Our ‘divergent’ timescale would be cut off.

We can compare the long time state - characterised by an added energy  $\Delta\mathcal{E}(E_0)$  - with what arises in a equilibrium thermal situation with the same energy  $\Delta\mathcal{E}(T)$ . The equilibrium ‘excess energy’  $\Delta\mathcal{E}(T) = \mathcal{E}(T) - \mathcal{E}(0)$  can be worked out from Monte Carlo or Langevin calculation on the electron-phonon system. Once the map from  $E_0$  to  $T$  is obtained we can compare the order parameter in the long time pumped state with a thermal state at the same excess energy. The comparison is in Fig.22. While the critical  $E_0$  estimate is reasonable, the actual thermal transition and the pump drive transition have the following difference. The suppression in  $|x_{\mathbf{Q}}|^2$

in the photo-pump case is due to the amplitude suppression but the suppression in  $|x_{\mathbf{Q}}|^2$  in thermal case is more like, where the  $x_i$  amplitude distribution remains roughly similar at zero and finite temperature but interference between domains leads to loss of long range order.

## VIII. CONCLUSIONS

We have studied the effect of a short laser pulse on a charge ordered system, realised in the two dimensional half filled spinless Holstein model. We work at intermediate electron-phonon coupling, roughly  $\sim 40\%$  of the coupling needed for a single polaron formation, and study the coupled dynamics of the lattice variables ( $x_i$ ) and the electronic correlator  $\rho_{ij}(t) = \langle c_i^\dagger(t)c_j(t) \rangle$  within a mean-field dynamics scheme. The method is nonperturbative in electron-phonon coupling and handles spatial correlations exactly. The dynamics can be categorized into three regimes with increasing pulse strength. At weak pulse strength we find a small oscillatory suppression of the order parameter to a finite long time value. At intermediate pulse strength (which we label as the critical regime) the dynamics show strong suppression and revival of the order parameter. This involves a rapid drop of the order parameter to almost zero, where the system stays for a time  $\sim \tau_{cr}$ , and then a power law rises to a finite long-time value. We find that  $\tau_{cr} \rightarrow \infty$  and the long time value  $\rightarrow 0$ , as the pulse strength  $E_0$  tends to a critical value  $E_0^c$ . This defines a nonequilibrium phase transition. We have established the transition by studying the system on accessible lattice size (up to  $20 \times 20$ ) and time windows. For a strong pulse, the CO order parameter decays monotonically to zero. Associated with the CO order parameter behavior is an gap closing and re-opening transition in the critical regime and a gap closing transition in the strong pulse regime. Since full mean field dynamics is expensive on large lattices we constructed an effective classical model for the phonons where the phonon dynamics is driven by a nonequilibrium electron population derived from MFD. This model captures all the three regimes that one sees in MFD and provides better access to critical properties than MFD does. Both MFD and the classical model suffer from lack of equilibration between electrons and phonons and our results would be modified when these ‘beyond mean field’ effects are incorporated. We provide an estimate of this timescale.

*Acknowledgment:* We acknowledge the use of the HPC clusters at HRI.

- 
- [1] J. Bloch, A. Cavalleri, V. Galitski, *et al.*, Strongly correlated electron–photon systems, *Nature* **606**, 41–48 (2022).  
 [2] E. Beaupaire, J.-C. Merle, A. Daunois, and J.-Y. Bigot, Ultrafast spin dynamics in ferromagnetic nickel, *Phys. Rev. Lett.* **76**, 4250 (1996).  
 [3] E. Carpena, E. Mancini, C. Dallera, M. Brenna, E. Puppini, and S. De Silvestri, Dynamics of electron-magnon interaction and ultrafast demagnetization in thin iron films, *Phys. Rev. B* **78**,

174422 (2008).

- [4] P. Beaud, S. L. Johnson, E. Vorobeva, U. Staub, R. A. De Souza, C. J. Milne, Q. X. Jia, and G. Ingold, Ultrafast structural phase transition driven by photoinduced melting of charge and orbital order, *Phys. Rev. Lett.* **103**, 155702 (2009).  
 [5] M. Fiebig, K. Miyano, Y. Tomioka, *et al.*, Sub-picosecond photo-induced melting of a charge-ordered state in a perovskite manganite, *Appl Phys B* **71**, 211–215 (2000).



- [6] S. Iwai, M. Ono, A. Maeda, H. Matsuzaki, H. Kishida, H. Okamoto, and Y. Tokura, Ultrafast optical switching to a metallic state by photoinduced mott transition in a halogen-bridged nickel-chain compound, *Phys. Rev. Lett.* **91**, 057401 (2003).
- [7] H. Matsuzaki, H. Uemura, M. Matsubara, T. Kimura, Y. Tokura, and H. Okamoto, Detecting charge and lattice dynamics in photoinduced charge-order melting in perovskite-type manganites using a 30-femtosecond time resolution, *Phys. Rev. B* **79**, 235131 (2009).
- [8] M. Chávez-Cervantes, G. E. Topp, S. Aeschlimann, R. Krause, S. A. Sato, M. A. Sentef, and I. Gierz, Charge density wave melting in one-dimensional wires with femtosecond subgap excitation, *Phys. Rev. Lett.* **123**, 036405 (2019).
- [9] H. Okamoto, H. Matsuzaki, T. Wakabayashi, Y. Takahashi, and T. Hasegawa, Photoinduced metallic state mediated by spin-charge separation in a one-dimensional organic mott insulator, *Phys. Rev. Lett.* **98**, 037401 (2007).
- [10] D. Cho, S. Cheon, K. Kim, S. H. Lee, Y. H. Cho, S. W. Cheong, and H. W. Yeom, Nanoscale manipulation of the mott insulating state coupled to charge order in 1T-TaS<sub>2</sub>, *Nat. Comm* **7**, 10453 (2015).
- [11] H. Ichikawa, S. Nozawa, T. Sato, *et al.*, Transient photoinduced ‘hidden’ phase in a manganite, *Nature Mater* **10**, 101–105 (2011).
- [12] Q. M. Liu, D. Wu, Z. A. Li, *et al.*, Photoinduced multistage phase transitions in Ta<sub>2</sub>NiSe<sub>5</sub>, *Nat Commun* **12**, 2050 (2021).
- [13] M. Budden, T. Gebert, M. Buzzi, *et al.*, Evidence for metastable photo-induced superconductivity in K<sub>3</sub>C<sub>60</sub>, *Nat. Phys.* **17**, 611–618 (2021).
- [14] D. Fausti, R. I. Tobey, N. Dean, S. Kaiser, A. Dienst, M. C. Hoffmann, S. Pyon, T. Takayama, H. Takagi, and A. Cavalleri, Light-induced superconductivity in a stripe-ordered cuprate, *Science* **331**, 189 (2011).
- [15] T. Han, F. Zhou, C. Malliakas, P. Duxbury, S. Mahanti, M. Kanatzidis, and C.-Y. Ruan, Exploration of metastability and hidden phases in correlated electron crystals visualized by femtosecond optical doping and electron crystallography, *Science Advances* **1**, e1400173 (2015).
- [16] Y. Zhang, X. Shi, W. You, Z. Tao, Y. Zhong, F. Kabeer, P. Maldonado, P. Oppeneer, M. Bauer, K. Rossnagel, H. Kapteyn, and M. Murnane, Coherent modulation of the electron temperature and electron-phonon couplings in a 2d material, *Proceedings Of The National Academy Of Sciences* **117**, 8788 (2020).
- [17] J. Maklar, Y. W. Windsor, C. W. Nicholson, *et al.*, Nonequilibrium charge-density-wave order beyond the thermal limit, *Nat Commun* **12**, 2499 (2021).
- [18] F. Schmitt, P. Kirchmann, U. Bovensiepen, R. Moore, J. Chu, D. Lu, L. Rettig, M. Wolf, I. Fisher, and Z. Shen, Ultrafast electron dynamics in the charge density wave material TbTe<sub>3</sub>, *New J. Phys* **13**, 063022 (2011).
- [19] L. Rettig, J. Chu, I. Fisher, U. Bovensiepen, and M. Wolf, Coherent dynamics of the charge density wave gap in tritellurides, *Phys. Rev. Lett.* **114**, 067402 (2014).
- [20] S. Hellmann, M. Beye, C. Sohrt, T. Rohwer, F. Sorgenfrei, H. Redlin, M. Kallane, M. Marczyński-Buhlow, F. Hennies, M. Bauer, A. Fohlisch, L. Kipp, W. Wurth, and K. Rossnagel, Ultrafast melting of a charge-density wave in the mott insulator 1T-TaS<sub>2</sub>, *Phys. Rev. Lett.* **105**, 187401 (2010).
- [21] E. Carpene, E. Mancini, C. Dallera, G. Ghiringhelli, C. Manzoni, G. Cerullo, and S. D. Silvestri, A versatile apparatus for time-resolved photoemission spectroscopy via femtosecond pump-probe experiments, *Rev. Sci. Instrum.* **80**, 055101 (2009).
- [22] J. Sobota, Y. He, and Z. Shen, Angle-resolved photoemission studies of quantum materials, *Rev. Mod. Phys.* **93**, 025006 (2021).
- [23] S. Eich, A. Stange, A. Carr, J. Urbancic, T. Popmintchev, M. Wiesenmayer, K. Jansen, A. Ruffing, S. Jakobs, T. Rohwer, S. Hellmann, C. Chen, P. Matyba, L. Kipp, K. Rossnagel, M. Bauer, M. Murnane, H. Kapteyn, S. Mathias, and M. Aeschlimann, Time- and angle-resolved photoemission spectroscopy with optimized high-harmonic pulses using frequency-doubled ti:sapphire lasers, *Journal of Electron Spectroscopy and Related Phenomena* **195**, 231 (2014).
- [24] N. Gedik and I. Vishik, Photoemission of quantum materials, *Nature Phys* **13**, 1029–1033 (2017).
- [25] C. Jia, K. Wohlfield, Y. Wang, B. Moritz, and T. P. Devereaux, Using rixs to uncover elementary charge and spin excitations, *Phys. Rev. X* **6**, 021020 (2016).
- [26] M. Mitrano and Y. Wang, Probing light-driven quantum materials with ultrafast resonant inelastic x-ray scattering, *Commun Phys* **3**, 184 (2020).
- [27] M. Rechtsman, J. Zeuner, Y. Plotnik, and *et al.*, Photonic floquet topological insulators, *Nature* **496**, 196–200 (2013).
- [28] T. Oka and S. Kitamura, Floquet engineering of quantum materials, *Annual Review of Condensed Matter Physics* **10**, 387 (2019).
- [29] M. Bukov, L. D’Alessio, and A. Polkovnikov, Universal high-frequency behavior of periodically driven systems: from dynamical stabilization to floquet engineering, *Advances in Physics* **64**, 139–226 (2015).
- [30] H. Frohlich, Electrons in lattice fields, *Adv. Phys.* **3**, 325 (1954).
- [31] E. K. H. Salje, A. S. Alexandrov, and W. Y. Liang, *Polarons and Bipolarons in High Temperature Superconductors and Related Materials* (Cambridge University Press, 1995).
- [32] C. Franchini, M. Reticcioli, M. Setvin, and *et al.*, Polarons in materials, *Nat Rev Mater* **6**, 560–586 (2021).
- [33] C. P. Adams, J. W. Lynn, Y. M. Mukovskii, A. A. Arsenov, and D. A. Shulyatev, Charge ordering and polaron formation in the magnetoresistive oxide La<sub>0.7</sub>Ca<sub>0.3</sub>MnO<sub>3</sub>, *Phys. Rev. Lett.* **85**, 3954 (2000).
- [34] O. Bradley, G. Batrouni, and R. Scalettar, Superconductivity and charge density wave order in the two-dimensional holstein model, *Phys. Rev. B* **103**, 235104 (2021).
- [35] R. McKenzie, C. Hamer, and D. Murray, Quantum monte carlo study of the one-dimensional holstein model of spinless fermions, *Phys. Rev. B* **53**, 9676 (1996).
- [36] S. Pradhan and G. V. Pai, Holstein-hubbard model at half filling: A static auxiliary field study, *Phys. Rev. B* **92**, 165124 (2015).
- [37] C. W. Chen, J. Choe, and E. Morosan, Charge density waves in strongly correlated electron systems, *Rep. Prog. Phys.* **79**, 084505 (2016).
- [38] N. C. Costa, K. Seki, S. Yunoki, and S. Sorella, Phase diagram of the two-dimensional hubbard-holstein model, *Communications Physics* **3**, 80 (2020).
- [39] A. Vernes and P. Weinberger, Formally linear response theory of pump-probe experiments, *Phys. Rev. B* **71**, 165108 (2005).
- [40] J. Bunemann and G. Seibold, Charge and pairing dynamics in the attractive hubbard model: Mode coupling and the validity of linear-response theory, *Phys. Rev. B* **96**, 245139 (2017).
- [41] J. K. Freericks, H. R. Krishnamurthy, and T. Pruschke, Theoretical description of time-resolved photoemission spectroscopy: Application to pump-probe experiments, *Phys. Rev. Lett.* **102**, 136401 (2009).
- [42] M. Eckstein and M. Kollar, Measuring correlated electron dynamics with time-resolved photoemission spectroscopy, *Phys. Rev. B* **78**, 245113 (2008).

- [43] G. Khitrova, P. R. Berman, and M. Sargent, Theory of pump-probe spectroscopy, *J. Opt. Soc. Am. B* **5**, 160 (1988).
- [44] P. Dolgirev, A. Rozhkov, A. Zong, A. Kogar, N. Gedik, and B. Fine, Amplitude dynamics of the charge density wave in  $\text{LaTe}_3$ : Theoretical description of pump-probe experiments, *Phys. Rev. B* **101**, 054203 (2020).
- [45] P. Dolgirev, M. Michael, A. Zong, N. Gedik, and E. Demler, Self-similar dynamics of order parameter fluctuations in pump-probe experiments, *Phys. Rev. B* **101**, 174306 (2020).
- [46] J. Okamoto, Time-dependent spectral properties of a photoexcited one-dimensional ionic hubbard model: an exact diagonalization study, *New J. Phys.* **21**, 123040 (2019).
- [47] B. Moritz, T. P. Devereaux, and J. K. Freericks, Time-resolved photoemission of correlated electrons driven out of equilibrium, *Phys. Rev. B* **81**, 165112 (2010).
- [48] O. P. Matveev, A. M. Shvaika, T. P. Devereaux, and J. K. Freericks, Time-domain pumping a quantum-critical charge density wave ordered material, *Phys. Rev. B* **94**, 115167 (2016).
- [49] M. D. Petrovic, M. Weber, and J. K. Freericks, Theoretical description of time-resolved photoemission in charge-density-wave materials out to long times, arXiv preprint arXiv:2203.11880 (2022), <https://arxiv.org/abs/2203.11880>.
- [50] M. Weber and J. K. Freericks, Real-time evolution of static electron-phonon models in time-dependent electric fields, *Phys. Rev. E* **105**, 025301 (2022).
- [51] J. Luo and G. W. Chern, Dynamics of electronically phase-separated states in the double exchange model, *Phys. Rev. B* **103**, 115137 (2021).
- [52] S. Bhattacharyya, S. S. Bakshi, S. Pradhan, and P. Majumdar, Strongly anharmonic collective modes in a coupled electron-phonon-spin problem, *Phys. Rev. B* **101**, 125130 (2020).
- [53] S. Bhattacharyya, S. S. Bakshi, S. Kadge, and P. Majumdar, Langevin approach to lattice dynamics in a charge-ordered polaronic system, *Phys. Rev. B* **99**, 165150 (2019).
- [54] N. Strohmaier, D. Greif, R. Jördens, L. Tarruell, H. Moritz, T. Esslinger, R. Sensarma, D. Pekker, E. Altman, and E. Demler, Observation of elastic doublon decay in the fermi-hubbard model, *Phys. Rev. Lett.* **104**, 080401 (2010).
- [55] Z. Lenarčič and P. Prelovšek, Ultrafast charge recombination in a photoexcited mott-hubbard insulator, *Phys. Rev. Lett.* **111**, 016401 (2013).